



Solid-state decomposition following partitionless solidification in dendrite arms of rapidly solidified CoCrCuFeNi_{0.8} high-entropy alloy

L.S.E. Teggins^{*} , R.F. Cochrane, S.L. Micklethwaite, Z.P. Aslam , A.E. Nassar, A.M. Mullis 

School of Chemical and Process Engineering, University of Leeds, Leeds LS2 9JT, United Kingdom

ARTICLE INFO

Keywords:

Rapid solidification
High-entropy alloy
Solid-state decomposition
Partitionless solidification
Spinodal decomposition

ABSTRACT

Partitionless solidification is a relatively understudied phenomenon in high-entropy alloys. In this study, a two-phase FCC CoCrCuFeNi_{0.8} high-entropy alloy was subjected to containerless rapid solidification in a drop-tube. The resultant droplets solidified at liquid phase cooling rates between 600 K s⁻¹ and 60,000 K s⁻¹. In a substantial portion of solidified droplets, the cores of solidified CoCrFeNi-rich primary dendrites were found to contain Cu-rich spherical dispersoids of similar composition to the Cu-rich interdendritic phase formed from rejected copper during solidification. The average composition of the decomposed regions of these dendrites matches the composition of the starting alloy and does not vary with droplet cooling rate. We reason that droplets featuring these dispersoids were undercooled below the T₀ temperature when in freefall in the liquid state. This caused the first dendrites to form via partitionless solidification. These regions became supersaturated as the droplet cooled further and likely underwent spinodal decomposition in the solid state. We also use CALPHAD modelling to estimate the solid phase spinode in the CoCrCuFeNi_{0.8} alloy, arguing that the required precursor to spinodal decomposition is likely a dendrite core that has become supersaturated with copper after partitionless solidification. The consistency in average composition of the decomposed dendrites at every cooling rate provides substantial evidence that this high-entropy alloy underwent undercooling mediated partitionless solidification rather than severe kinetic solute trapping. Furthermore, this work provides an analysis of conditions which may favour partitionless solidification in high-entropy alloys.

1. Introduction

Solid-state decomposition reactions in high-entropy alloys have been readily observed and have often occurred after long-term heat treatment processes such as annealing. For example, the single-phase FCC (face-centred cubic) equiatomic CoCrFeMnNi alloy, or Cantor alloy, has been found to decompose into up to four other phases (σ , BCC, B2 and L1₀) upon prolonged heat treatment at key temperatures of 500 °C and 700 °C after 500 days [1]. The authors suggest that this is due to thermodynamic instability below about 800 °C. Presumably, the decomposition reactions that occur below this temperature are suppressed kinetically when the alloy is cooled to room temperature. After heat treatment at 800 °C to 900 °C, equiatomic TiZrNbHfTa alloys, in the form of nanocrystals, have also been observed to decompose from single-phase BCC into a dual-phase BCC structure, with a further HCP phase forming, in some cases, at lower heat treatment temperatures [2]. Similar solid-state decomposition reactions have been observed during annealing of multiple specific alloys within the compositional family of Al-Cr-Nb-Ti-V-Zr

alloys by Yurchenko et al. [3,4] and, more recently, in AlCuNiPdPt [5,6].

Interestingly, solid-state decomposition reactions have also been observed in HEAs during the initial solidification process, without the need for long-term heat treatment. Munitz et al. [7] cast AlCrFeMnNi alloys, showing that the dendritic and interdendritic phases that formed upon solidification both decomposed spinodally upon further cooling to room temperature. The same seemingly also occurs in AlCoCrFeNi [8,9]. A solid-state miscibility gap is hypothesized to be present in an FCC solid solution phase of Al_{0.5}CoCrCuFeNi, causing the phase to decompose spinodally after casting [10]. The authors have hence suggested that it is not possible to suppress this reaction, even at very high cooling rates. The spinodal character of the decomposition is verifiable through rapid solidification experiments on similar alloys. Singh et al. [11] processed equiatomic AlCoCrCuFeNi by conventional casting and splat quenching with cooling rates of 10 – 20 K s⁻¹ and 10⁶ – 10⁷ K s⁻¹ respectively. Casting caused the solidified dendrites in AlCoCrCuFeNi to decompose extensively into multiple phases. However, the authors point out that even the seemingly uniform regions in the microstructure of the

^{*} Corresponding author.

E-mail address: pm15lset@leeds.ac.uk (L.S.E. Teggins).

<https://doi.org/10.1016/j.actamat.2025.120858>

Received 22 September 2024; Received in revised form 13 February 2025; Accepted 20 February 2025

Available online 21 February 2025

1359-6454/© 2025 The Authors. Published by Elsevier Inc. on behalf of Acta Materialia Inc. This is an open access article under the CC BY license (<http://creativecommons.org/licenses/by/4.0/>).

splat-quenched sample featured nanosized domain structures in the grain centres, indicating the initial stages of phase decomposition.

In many cases, decomposition of an alloy in the solid state during solidification is associated with an initial solid phase becoming supersaturated with solute during cooling. This supersaturation can be brought on by non-equilibrium cooling of the initial liquid, where solute cannot partition as it would during equilibrium solidification. This “solute trapping” is often explained by examining solidification kinetics. During dendritic solidification of a liquid alloy, the growth velocity of the solid dendrites is directly affected by the degree of undercooling. Such a dependence has been studied in pure metals [12–15], intermetallic compounds [16], conventional alloys [13,14,17], and even HEAs such as equiatomic CoCrCuFeNi [18]. In all cases, a higher undercooling of the parent liquid results in a higher maximum dendrite growth velocity during solidification. As growth velocity increases, the velocity of the solid phase growth front becomes too rapid for solute to diffuse across the solid-liquid interface before solidification, trapping solute in the solid phase. The resultant solid is enriched in solute compared to if it were solidified at equilibrium conditions. A prominent kinetic model of this effect is the continuous growth model (CGM) for dilute alloys created by Aziz [19] and generalised by Aziz and Kaplan [20] for solutions of any composition. In models such as these, the nature of partitioning is defined in terms of a partition coefficient k . With increasing dendrite growth velocity V , the solute partition coefficient k (for a phase diagram with negative liquidus slope, a value between 0 and unity) increases from a value at equilibrium, k_e , and asymptotically tends towards unity as dendrite growth velocity V becomes much larger than the diffusion rate for solute across the interface V_{D_i} . As the partition coefficient approaches unity ($k \rightarrow 1$), we reach a stage of near complete solute trapping, where the composition of the growing solid has almost the same composition as the initial liquid. With a partition coefficient of k_e , solute partitioning across the solid and liquid would occur as it would under equilibrium conditions. The generalised CGM proposed by Aziz and Kaplan [20] is shown in Eq. (1) for the calculation of partition coefficient at a given interface growth velocity $k_{CGM}(V)$. Here, X_L is the atomic fraction of solute in the liquid at the interface. For a dilute alloy, $X_L \ll 0$ and hence $(1 - k_e)X_L \ll 0$. The equation thus simplifies to that given by Aziz [19]. Solute concentration profiles estimated based on the CGM were supported experimentally in subsequent studies on aluminium alloys and Si-As [21–23].

$$k_{CGM}(V) = \frac{k_e + V / V_{D_i}}{V / V_{D_i} + 1 - (1 - k_e)X_L} \quad (1)$$

In contrast to solute partitioning brought on by non-equilibrium solidification where $0 < k < 1$, some studies have attributed solid-state decomposition in alloys to the formation of metastable precursor phases via completely partitionless solidification. In this scenario, the initial solid phase formed has the same composition as the liquid from which it solidifies. Entirely partitionless solidification was first shown by Baker and Cahn to be thermodynamically possible [24]. However, there are thermodynamic conditions upon which the possibility of partitionless solidification is dependent. Crucially, the temperature at the interface between the growing solid and the residual liquid must be below the T_0 line of the alloy phase diagram at the composition of the liquid. Below this line, the requirement of a reduction in free energy during transformation from liquid to solid is satisfied without a change in the composition between solid and liquid [25].

The occurrence of partitionless solidification is linked with the transition between growth of the solid controlled by solute diffusion to complete control by heat diffusion as dendrite growth velocity increases. Willnecker et al. [26] studied this effect in Cu-Ni alloys and point out that kinetic solute trapping models such as the CGM accurately predict solute partitioning results only below a critical dendrite growth velocity (brought on by a critical undercooling below the liquidus ΔT^*). Eckler et al. [27] have also shown this transition occurring in Ni-B alloys,

resulting in partitionless solidification occurring at undercoolings above ΔT^* . Importantly, they also note that this critical undercooling depends heavily on alloy composition.

Two key shortcomings are therefore evident in the CGM. These are the ability to accurately predict solute trapping behaviour only at relatively low dendrite growth velocities, and a lack of representation of the transition to complete solute trapping ($k = 1$) when interface growth velocity exceeds a finite value, which has been previously observed in experiments. Such issues are treated in later kinetic models. The local non-diffusion model (LNDM) suggested by Sobolev [28–31] addresses this issue for dilute alloys through a distinction between the velocity of diffusion of solute across the interface V_{D_i} (discussed by Aziz and Kaplan) and that of diffusion of solute in the bulk V_{D_b} . Initially, the model works similarly to the CGM, with partition coefficient increasing as $V \rightarrow V_{D_i}$. However, because generally, $V_{D_b} > V_{D_i}$, a limit of completely partitionless solidification is proposed when $V > V_{D_b}$. Once this condition is fulfilled, $k = 1$. [29]. This model is described in Eq. (2) and calculates the partition coefficient for a specific interface growth velocity V .

$$k_{LNDM}(V) = \begin{cases} \frac{k_e + \left(1 - V^2 / V_{D_b}^2\right) + V / V_{D_i}}{\left(1 - V^2 / V_{D_b}^2\right) + V / V_{D_i}}, & V < V_{D_b} \\ 1, & V > V_{D_b} \end{cases} \quad (2)$$

A further model proposed by Galenko [32] generalises the LNDM for any concentration of solute in the liquid and unites the limit cases yielded in the CGM and LNDM models. Eq. (3) calculates the partition coefficient using this model for a specific initial alloy solute content X_0 and interface growth velocity V . At low interface growth velocities where $V < V_{D_b}$ and for a dilute alloy where $(1 - k_e)X_0 \ll 1$, the partition coefficient is defined as it would be by the LNDM. In the limit case where the diffusion of solute in the bulk liquid is very quick ($V_{D_b} \rightarrow \infty$), we arrive at the solution proposed by the Aziz-Kaplan CGM. When $V > V_{D_b}$, complete solute trapping occurs, and the partition coefficient becomes 1.

$$k_{GAL}(V, X_0) = \begin{cases} \frac{\left(1 - V^2 / V_{D_b}^2\right) [k_e - (1 - k_e)X_0] + V / V_{D_i}}{\left(1 - V^2 / V_{D_b}^2\right) + V / V_{D_i}}, & V < V_{D_b} \\ k_{GAL}(V, X_0) = 1, & V \geq V_{D_b} \end{cases} \quad (3)$$

This model is much more descriptive of solute trapping behaviour in Si-As alloys [22,23] than previous work, particularly at high interface velocities approaching the critical velocity for partitionless growth.

In more conventional alloys, the thermodynamic argument (based on the T_0 temperature) has been invoked to explain regions in the solidified microstructure where average composition is almost exactly equal to the initial alloy composition (within measurement instrument error). In 1991, Cantor et al. [33] studied melt-spun Ni-5wt% Al and 316 L stainless steel. Early in the solidification process, they observe columnar solidification with a plane front that they describe as partitionless, attributing this to a high undercooling brought on by the melt-spinning process, which increases growth velocity. This condition only occurs in the initial solid formed in the dendrite cores and is no longer satisfied later in the solidification process. The transition from partitionless growth to partitioning is thought to occur following the consistent release of latent heat and corresponding increase in interface temperature. McKeown et al. [34,35] solidified eutectic U-6wt% Nb particles via centrifugal atomisation, yielding droplets between 155 μm and 1 μm . Calculated cooling rates achieved were between 10^3 and 10^8 K s^{-1} . Interestingly the authors observe dendritic and non-dendritic regions in the droplets which vary in prominence with decreasing droplet size. In smaller droplets, large non-dendritic regions are observed which, along with interdendritic regions, possess a composition very close to the initial liquid composition. The prevalence of the non-dendritic region

increases with increasing cooling rates. The authors attribute this to a partitionless solidification brought on by large prevailing undercoolings in the rapidly cooling droplets. This partitionless solidification ceases once recalescence causes the droplet temperature to rise above a certain value, at which partitioning becomes evident. Galuskova et al. [36] observed that a cooling rate of 10^5 K s^{-1} suppresses the eutectic reaction in Bi-Sn alloys and causes partitionless solidification and subsequent solid-state decomposition on further cooling towards room temperature. In their work on drop-tube processed Al-3.9wt% Fe alloy droplets, Abul et al. [37] observe regions in droplets of all cooling rates between 100 K s^{-1} and $20,000 \text{ K s}^{-1}$ where composition is close to the composition of the original alloy. This is supported by the fact that undercoolings attainable in the drop-tube would be more than adequate to achieve the 42 K undercooling required to drop below T_0 in the alloy. In further work on Al-4.1wt% Fe-1.9wt% Si, they note areas in the droplets where partitionless solidification seems to have occurred for iron but not for silicon, which they suggest could be because iron and silicon diffuse at drastically different speeds in liquid aluminium [38]. Similar partitionless regions are observed in rapidly quenched Al-12.6wt% Si-0.8wt% Mg-0.4wt% Mn-0.7wt% Fe-0.9wt% Ni-1.8wt% Cu [39].

In HEAs, with many more component elements, partitionless solidification seems to be much more seldom encountered. In their work on a suction cast ZrNbAlTiV alloy, Vishwanadh et al. [40] measured the composition of a single-phase region in the solidified microstructure. This area was shown to have a composition near the composition of the initial liquid, which the authors attribute to partitionless solidification from the liquid. In their extensive work on Al-Ni-Cr-Fe-Mn alloys, Ananiadis et al. and Mathiou et al. [41,42] observed that dendrites in as-cast $\text{Al}_{10}\text{Cr}_{26.7}\text{Fe}_{26.7}\text{Mn}_{26.7}\text{Ni}_{10}$ and $\text{Al}_{14}\text{Cr}_{24}\text{Fe}_{24}\text{Mn}_{24}\text{Ni}_{14}$ had subsequently undergone decomposition in the solid state. They argue that the dendrites had initially solidified in a partitionless manner but had subsequently undergone spinodal decomposition into two phases after further cooling rendered the initially solidified phase thermodynamically unstable. Srimark et al. [43] investigated arc-melted $\text{Al}_{0.7}\text{CoCrFeNi}$ to establish a solidification pathway. They suggest a sequence where a B2 metastable phase which solidified in a partitionless manner from the melt subsequently decomposed into stable B2 and FCC phases. They also provide a CALPHAD simulation to support the conjecture that partitionless solidification is thermodynamically possible in this alloy. An investigation into unexpected spinodal decomposition in a $\text{Al}_{30}\text{Co}_{10}\text{Cr}_{30}\text{Fe}_{15}\text{Ni}_{15}$ eutectic HEA was undertaken through thermodynamic modelling by Bai et al. [44]. They suggest that the undercooling required for partitionless solidification in the alloy is lowered due to short-range order in the parent liquid and the high configuration entropy of the forming solid phase. This leads to partitionless growth of a metastable B2 phase in the melt, which undergoes a final spinodal decomposition as temperature decreases. Very recently, Yan et al. [45] investigated EML processed CoCrCuFeNi equiatomic alloy which undergoes liquid phase separation (LPS). They note that a decrease in volume fraction of a Cu-rich interdendritic phase between the CoCrFeNi-rich dendrites as undercooling increases provides evidence for a transition from growth controlled by diffusion of copper-solute to purely thermal diffusion-controlled growth. In droplets having undergone LPS, the CoCrFeNi-rich phase exhibits nearly no interdendritic copper, pointing to the occurrence of a near partitionless solidification at the highest undercoolings.

In this work, we discuss notable Cu-rich dispersions formed selectively in dendrite arm cores of rapidly solidified CoCrCuFeNi_{0.8} HEAs during the initial solidification processing in a drop-tube, without need for any subsequent heat treatment. We aim to characterise these dispersions in detail and suggest mechanisms for their formation. Through this, we work to further elucidate the behaviour of high-entropy alloys during rapid solidification in comparison to more conventional binary alloys.

2. Experimental methodology

2.1. Sample preparation and microstructural analysis

An alloy ingot of CoCrCuFeNi_{0.8} was formed by successive arc-melting of the pure metal constituents. Cobalt, chromium, copper, iron and nickel, in the form of rod or shot, were sourced at a purity of at least 99.0%. The starting components were gradually added together in stages. During formation of each intermediate alloy, the arc-melted button was melted, removed from the arc-melter, sanded to remove any external oxide layer formed, and flipped from its original orientation in the arc-melter before re-melting. This process was repeated at least three times for each step. The intermediate alloys created were CoFe, CuNi_{0.8}, and quaternary CoCuFeNi_{0.8}. Chromium was added last to form the final CoCrCuFeNi_{0.8} alloy. Oxidation during melting, and subsequent sanding with SiC paper to remove this oxide layer after each melt, resulted in a loss of 3.9 g of material. The final button shaped ingot weighed 16.5 g.

8.1 g of the formed ingot was drop-tube processed. Drop-tube processing is a form of rapid solidification processing where liquid metal is ejected through a small orifice, dispersing into droplets. These liquid droplets then solidify in freefall through a low-pressure inert gas atmosphere. For the sake of brevity, more detailed explanations of the principles behind drop-tube processing and descriptions of the specific apparatus at the University of Leeds are provided in [46]. Collected droplets were sieved into size fractions of 850+, 850–500, 500–300, 300–212, 212–150, 150–106, 106–75, 75–53, and 53–38 μm . Droplets from each size fraction were cold-mounted in resin, while a section of the original arc-melted ingot was hot-mounted. Sample grinding was completed using P400 and P1200 SiC paper as well as 3 μm and 1 μm diamond paste polish. 0.05 μm colloidal silica was used in the final polishing step.

2.2. Calculation of droplet cooling rate

Given the fast pace of the drop-tube experiment and the thousands of droplets of different size and morphology that are produced immediately after ejection, it is impossible to accurately measure the instantaneous temperature of a specific droplet. Therefore, a theoretical heat transfer model for a spherical metal droplet in free-fall through a gaseous atmosphere has been developed to determine the prevailing cooling rate for each droplet diameter. We define an energy balance across the droplet-gas interface through Eq. (4), where T_d is the instantaneous droplet temperature, dT_d/dt is the overall prevailing droplet cooling rate, $c_{p(l)}$ is the liquid phase specific heat capacity, f is the volume fraction solidified, $c_{p(s)}$ is the solid phase specific heat capacity, $L_{f(\text{alloy})}$ is the latent heat of solidification of the alloy, h is the convective heat transfer coefficient, ρ_{alloy} is the alloy melt density, d is the droplet diameter, ε is the surface emissivity of the alloy droplet (assumed to be the same for solid and liquid phases), σ_b is the Stefan-Boltzmann constant, and T_g is the gas temperature:

$$\frac{dT_d}{dt} \left[c_{p(l)}(1-f) + c_{p(s)}f - L_{f(\text{alloy})} \frac{df}{dt} \right] = \frac{6h}{\rho_{\text{alloy}}d} (T_d - T_g) + \frac{6\varepsilon\sigma_b}{\rho_{\text{alloy}}d} (T_d^4 - T_g^4) \quad (4)$$

The overall cooling rate dT_d/dt factors in the liquid phase cooling rate, solidification and the solid phase cooling rate once the droplet has fully solidified. More detailed derivation of the specific terms in the above equation can be found in [46–48]. For the purposes of this investigation, we are most concerned with the maximum cooling rates occurring in the liquid and solid states respectively (i.e. when $f = 0$ and $f = 1$). In both cases, the droplet is only single phase, so $df/dt = 0$. The maximum liquid and solid phase cooling rates $dT_{d(l)}/dt$ and $dT_{d(s)}/dt$ are thus determined through Eq. (5).

$$\frac{dT_{d(l,s)}}{dt} = \frac{1}{c_{p(l,s)}} \left\{ \frac{6h}{\rho_{\text{alloy}(l,s)} d} (T_d - T_g) + \frac{6\epsilon\sigma_b}{\rho_{\text{alloy}(l,s)} d} (T_d^4 - T_g^4) \right\} \quad (5)$$

2.3. Microstructural analysis

Initial microstructural surveys were performed using a Carl Zeiss LSM800 Mat CLSM confocal optical microscope. Further detailed microstructural analysis was conducted using a Hitachi SU8230 SEM. The EDX attachment on the SEM was used for composition analysis. More selective EDX analysis was conducted within specific regions of interest within the microstructure. These regions were defined by a closed freehand drawn area.

A small section of one droplet (212 – 150 μm size fraction) was removed using a FEI – Helios G4 CX Dual beam FIBSEM. The final FIB section had a thickness of 80 – 90 nm and was used for targeted analysis of the nano-scale structure of the alloy. This was conducted using a FEI Titan Cubed Themis 300 G2 FEG S/TEM operated at 300kV. Bright field TEM (BFTEM) images were collected using the GATAN OneView 16 Megapixel CMOS digital camera. Next, the fitted Super-X EDX system with windowless 4-detector design and 0.7 srad solid angle was used to attain an understanding of the composition of the phases present in the microstructure. Finally, selected area electron diffraction (SAED) patterns for each principal phase were gathered for the purposes of comparison. ImageJ© software was used to determine spacing and angles between SAED diffraction points to determine phase crystal structure and interplanar spacings. These values include an uncertainty of 4 % due to instrumentation systematic error such as inaccurate camera constants or lens distortion as well as random error during visual measurement of the distances between diffraction points. However, if the interplanar spacings are calculated based on measurements from two adjacent regions taken contemporaneously, the error in these measurements reduces and is likely closer to 1 %. This is due to the consistency in systematic error across both measurements. The uncertainty inherent during measurement is determined via well-defined calibration protocols undertaken for the TEM microscope used in this investigation as recommended by the manufacturers.

2.4. Structural occurrence rate

In each size fraction, a minimum of 250 droplets were categorised in terms of microstructural morphology to better understand the trend in occurrence rate of various microstructures with alloy cooling rate. Over a dozen structures were defined and their occurrence rate logged through analysis of large-scale stitched images made from the optical images taken with the Carl Zeiss LSM800 Mat CLSM confocal microscope. Detailed analysis of this methodology, including selection of minimum sample size is reported in [49]. Definitions of each microstructure encountered during microscopic analysis of the CoCrCuFeNi_{0.8} droplets, along with SEM micrographs showing examples of each microstructure observed, are available in the supplementary information (Online Resource 1). For this particular study, we focus specifically on the occurrence, or not, of fine spherical dispersions of a Cu-rich phase within the primary, secondary or tertiary arms of CoCrFeNi-rich dendrites that grow into the liquid during solidification. We use the results of this statistical analysis to determine the occurrence rate of Cu-rich dispersoids in droplets of each size fraction following the methodology outlined in the supplementary information (Online Resource 1).

2.5. Cu-rich dispersoids area percentage

In addition to the occurrence rate of Cu-rich dispersoids covered in Section 2.4, at least three droplets from each size fraction which had solidified exclusively in a dendritic manner, and which feature Cu-rich dispersoids in dendrite arms, were selected for further analysis. For each droplet, the ImageJ© photo editing software was used to manually

delineate the areas in which Cu-rich dispersoids were present throughout the viewable droplet cross-sectional area (the area exposed during the polishing process). The area fraction of the droplet occupied by these dispersoids was then calculated by dividing the total area occupied by Cu-rich dispersoids by the total viewable droplet cross-sectional area. This was multiplied by 100 to calculate the area percentage occupied by Cu-rich dispersoids and an average was calculated for each droplet size fraction.

3. Results

3.1. Overall composition analysis

Table 1 indicates that the arc-melted sample of CoCrCuFeNi_{0.8} possesses a composition close to the calculated values based on the desired elemental ratio. Composition does not change appreciably after drop-tube processing, even in some of the smallest droplets. This suggests that average composition of the droplets is essentially uniform with reducing droplet diameter. In both the ingot and droplets, the slightly higher than predicted chromium content is likely a result of the fact that Cr was the last element added during the melting process, meaning less of this material oxidised or was sanded away.

3.2. Calculation of droplet cooling rate

Fig. 1 shows the results of the maximum liquid and solid phase cooling rates for CoCrCuFeNi_{0.8} droplets while in freefall in the drop-tube via interrogation of Eq. (5). Liquid phase droplet cooling rates range from a minimum of 600 K s⁻¹ in the largest droplets and a maximum of 60,000 K s⁻¹ in the smallest droplets. Solid phase cooling rates range from 400 K s⁻¹ to 40,000 K s⁻¹ for droplets of a similar size profile to those described above. Liquid phase cooling rates are higher than corresponding solid phase cooling rates in a particular droplet size fraction due to the reduction in the maximum temperature difference between the solid or liquid melt and the gas atmosphere. In both solid and liquid phase cooling rates, droplet diameter and cooling rates can be related using a power law. Thermophysical data used to calculate cooling rate for each droplet size in both liquid and solid states is provided in the supplementary information (Online Resource 2). These values were either determined through experimentation or taken from [50–52].

3.3. Microstructure analysis

SEM analysis of drop-tube processed CoCrCuFeNi_{0.8} alloy droplets shows that the large majority of these droplets across all size fractions and thus, cooling rates, solidify in a dendritic manner. The dendrites are CoCrFeNi-rich and grow into a highly Cu-rich interdendritic liquid, which then solidifies at a lower melting point given the high percentage of copper present. However, in numerous cases, many of these CoCrFeNi-rich dendrite trunks are populated with Cu-rich spherical dispersoids. In these droplets, the dispersoids are overwhelmingly located in the primary dendrite arms. In much less common cases, they are also found in secondary and even tertiary dendrite arms. Due to the position of the dispersoids exclusively in the cores of dendrite arms

Table 1

Average atomic composition comparison between arc-melted ingot and drop-tube processed CoCrCuFeNi_{0.8}.

	Co /at%	Cr /at%	Cu /at%	Fe /at%	Ni /at%
Predicted	20.8	20.8	20.8	20.8	16.7
Ingot	20.72 ± 0.08	22.12 ± 0.03	20.70 ± 0.18	20.43 ± 0.06	16.03 ± 0.06
Droplets	20.56 ± 0.02	21.74 ± 0.07	20.55 ± 0.04	20.87 ± 0.06	16.29 ± 0.03
(d = 75–53 μm)					

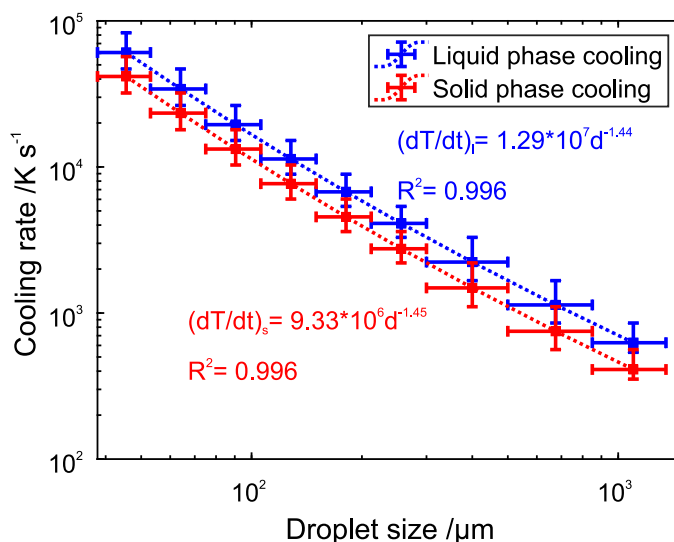


Fig. 1. Liquid phase and solid phase cooling rates for droplets of CoCrCuFeNi_{0.8} at varying droplet diameters.

rather than randomly throughout the microstructure, they are likely to have formed in the solid state after solidification of the dendrite in which they are located. The prevalence of these dispersions in the droplets is positively correlated with cooling rate. Examples of droplets with these dispersoids in the microstructure are shown in Fig. 2.

Fig. 2a and 2b represent, qualitatively, the difference in the extent to which dispersoids appear in dendrite cores of droplets of different sizes. Generally, a smaller droplet diameter (i.e. a higher prevailing cooling rate) seems to correspond to a greater extent of dispersoid prevalence, in that these spheres appear in more dendrites of an individual droplet as the theoretical droplet cooling rate increases. Fig. 2c shows the most common configuration of dispersions in the dendrites, where the cores of primary dendrites seem to be preferentially occupied before the secondary and tertiary dendrites. Indeed, we are unable to find any droplets where dispersions occupy secondary and tertiary dendrites without also being found in the corresponding primary dendrites. Some smaller droplets, such as those presented in Fig. 2d, have also been found with dispersions present in primary, secondary and tertiary dendrites. Overall, no matter what dendrites the dispersions are formed in, they are located overwhelmingly in the dendrite cores, and do not prevail across the entire dendrite cross section. A “buffer zone” is present between the dispersions in the dendrite cores and the interdendritic copper rich phase located between the dendrite arms. Fig. 2e shows the size distribution of the spherical dispersions in the dendrite cores. While, qualitatively, it seems as though the largest diameter dispersoids are located closer to the centre of the dendrite cross section, this trend is not absolute, with the size distribution of the dispersoids being mostly random and consistent across the dendrite diameter.

3.4. Trend in SSD occurrence and prevalence

Fig. 3 shows the variation in percentage occurrence and occupied area fraction of intradendritic dispersions in the alloy droplets across the size fractions. From this data, we see that by the time cooling rate increases above 10,000 K s⁻¹, incidence rate of dispersions in the dendrites is above 80 % and approaches a maximum of 95 % of all droplets at cooling rates of 20,000 K s⁻¹. Conversely, at the lowest cooling rates of about 1000 K s⁻¹, only about 5–10 % of droplets feature such dispersions. Similarly to the occurrence rate, the prevalence of dispersion regions as a percentage of the exposed droplet area also becomes more significant as cooling rate increases. At the lowest cooling rates below 2000 K s⁻¹, dispersed regions occupy an insignificant area fraction of the droplets in which they occur. The most significant increase in prevalence

of SSD occurs between 2000 K s⁻¹ and 8000 K s⁻¹ where the area fraction occupied jumps to 16–17 %. A plateau is then noticeable between 8000 K s⁻¹ and 40,000 K s⁻¹ after which, at the highest cooling rates near 60,000 K s⁻¹, the area fraction peaks at about 25 %.

3.5. Composition analysis

To determine how these dispersions were formed within the dendrites, we analyse the key differences between dendrites where dispersions prevail from those where they are absent. One area we can use to begin to differentiate these dendrites is composition data derived from the EDX mapping described in Section 2.3. Of particular importance to us is the status of the dendrite (i.e. whether it is primary or secondary) as well as whether dispersoids are found within the dendrite trunk. We therefore divided our compositional analysis to treat three different dendrites. Primary dendrites with dispersoids (PDD) and primary dendrites without dispersoids (PDND) define the two possible states of primary dendrite core morphology. The third category, secondary dendrites without dispersoids (SDND) consists of secondary dendrites (without Cu-rich spherical dispersoids) that branch from primary dendrites that do feature such dispersoids (PDD). To understand the average composition of the dendrite cores in each of these three defined configurations, we manually delineate a mask within the dendrite where EDX mapping will take place. In each droplet size fraction, at least three of each type of dendrite was analysed. The average at% values of each of the constituent elements was found and logged for four of the droplet size fractions yielded from the drop-tube experiment. These are the 500 – 300 μm, 300 – 212 μm, 212 – 150 μm, and 53 – 75 μm size fractions, encompassing the majority of the range of droplet sizes produced in the experiment. This process is shown in Fig. 4a, 4b and 4c for a PDD dendrite, PDND dendrite and SDND dendrite respectively. In all cases, we assume that the sample has a constant composition within the measured interaction volume.

Tables 2, 3, and 4 show average composition data gathered via EDX mapping analysis on the manually defined core regions of different classes of dendrites in CoCrCuFeNi_{0.8} droplets of varying diameters. Notably, in the PDD dendrites in Table 2, the composition values indicate an average composition which factors in both the Cu-rich dispersoids and the CoCrFeNi-rich matrix in which they are located.

From data shown in Tables 3 and 4, we argue that there is no significant difference between the composition of the PDND and SDND dendrites. For a chosen size fraction, any difference between in composition between these is accounted for by the calculated standard

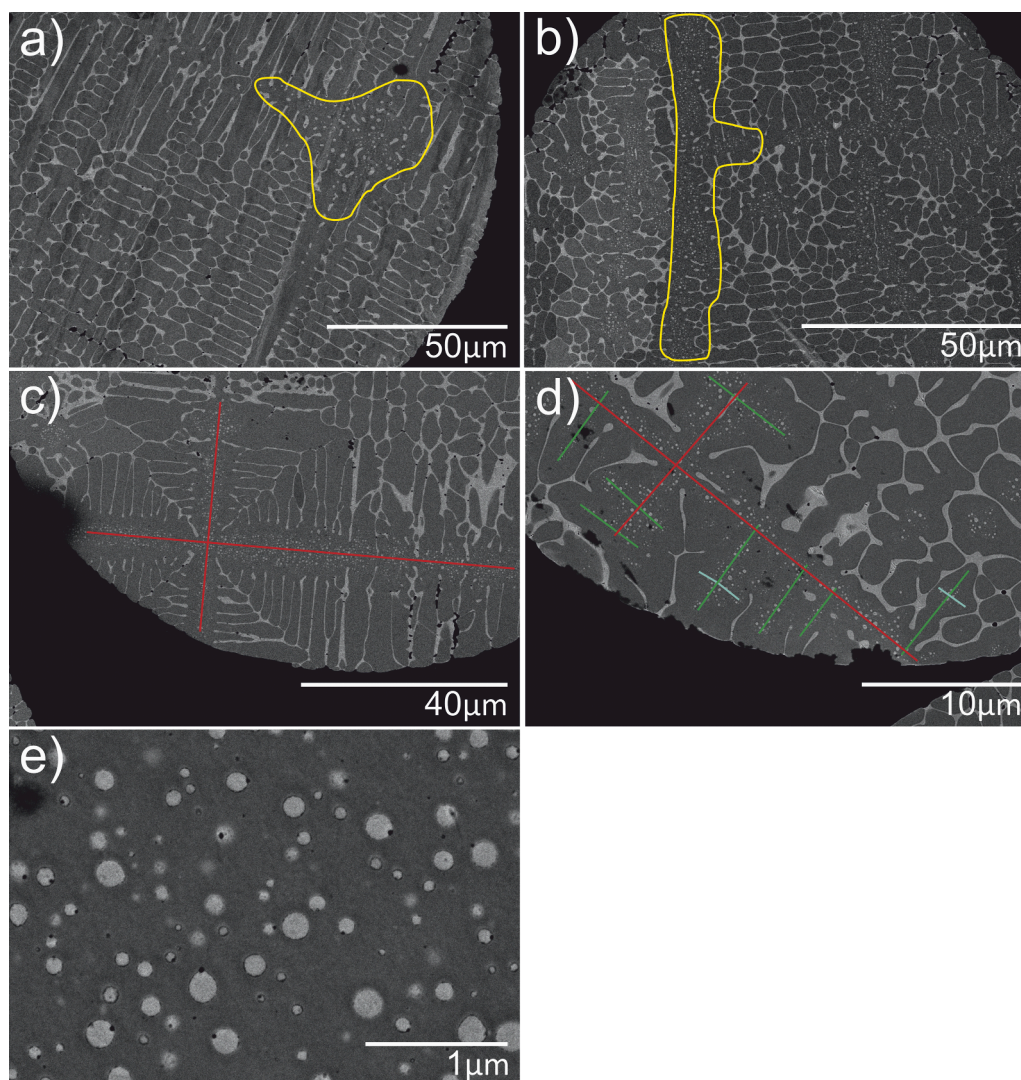


Fig. 2. Intradendritic spherical dispersions present in droplets of drop-tube processed CoCrCuFeNi_{0.8}. a. 212 – 150 μm droplet showing smallest extent of dispersoids (centre of yellow region) forming exclusively at dendrite nucleation point b. 150 – 106 μm droplet showing extensive prevalence of spherical dispersoids (e.g. yellow region) in dendrite cores across entire microstructure c. 150 – 106 μm droplet showing intradendritic dispersoids present exclusively in primary dendrites (red) d. 53 – 38 μm droplet showing spherical dispersoids present in primary (red), secondary (green) and tertiary (cyan) dendrites within droplet microstructure e. high magnification view of dispersoid size distribution in primary dendrite core of a 53 – 38 μm droplet.

error. This suggests any discrepancies are the result of random error from instrumentation rather than a systematic difference in composition. Note that, because nearly all primary dendrites in the smallest size fractions are populated with dispersoids, insufficient data was available to collect regarding the compositions of primary dendrites with no dispersoids present (PDND) in small droplets. Therefore, in Table 3, compositions of PDND dendrites in the 75 – 53 μm size fraction are marked with “no data”.

Importantly however, there is a marked difference between the average composition of PDND and SDND dendrites and that of the PDD dendrites (Table 2). Once dispersions are present in the case of the PDD dendrites, the atomic percentage of chromium, iron and cobalt decrease noticeably from 23 – 25 at% to between 20 – 22 at%. This decrease is balanced by an even more drastic increase in copper which rises from a range of 10.2 – 12.6 at% in PDND and SDND dendrites to 19.6 – 20.4 at% in the PDD dendrites. Finally nickel composition remains almost constant decreasing from a range of 17.0 – 16.7 at% to a range of 16.4 – 16.6 at%. This indicates a slightly lower amount of nickel in the PDD dendrites, but the change in nickel concentration is within the random error of the instrumentation, making this conclusion more tentative.

Strikingly, the average composition of the decomposed cores of the PDD dendrites (across all size fractions) is within the standard deviation error of the composition of the original alloy, indicating no substantial difference between these two compositions.

Furthermore, there is also no consistent increase or decrease in atomic percentage of any particular element as droplet size is reduced. In the large majority of cases, the composition values tend to fluctuate seemingly randomly within 1 – 2 at%, with the notable exception of the value of copper concentration in the undecomposed secondary dendrites (Table 4). We attribute this drastic increase in copper content from 10.5 at% to 12.6 at% as droplet size decreases to error caused by the relative increase in the interaction volume of the EDX X-rays compared to the smaller size of the dendrites in a droplet of 64 μm diameter compared to a droplet of 181 μm diameter. As dendrites decrease in size, a consistent volume of interaction may begin to detect the Cu-rich interdendritic phases adjacent to the dendrites.

3.6. TEM analysis – phase composition

Fig. 5a shows a TEM micrograph image of CoCrFeNi-rich dendrites

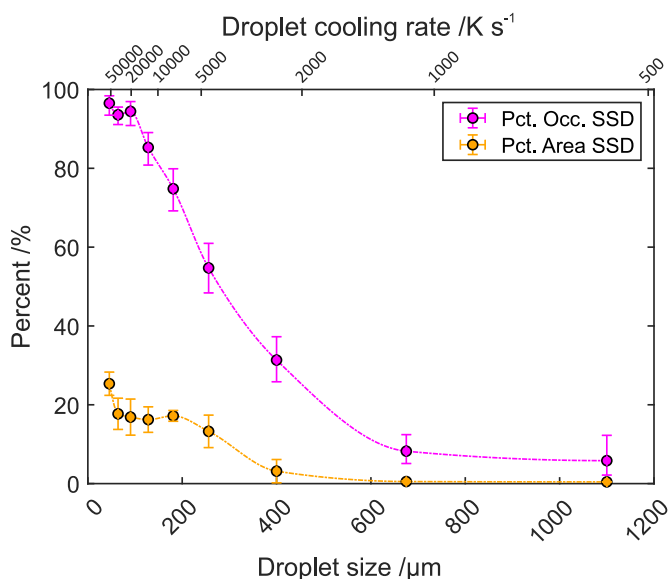


Fig. 3. Occurrence rate of (purple) and percent area occupied by (orange) fine intradendritic solid-state dispersions (SSD) in solidified droplet microstructures of drop-tube processed CoCrCuFeNi_{0.8} at varying droplet sizes and liquid phase cooling rates.

(A) and the Cu-rich interdendritic phase (B) between the dendrites. The selected area is located away from Cu-rich intradendritic dispersoids so that the composition of the dendritic phase is not impacted compositionally by proximity to an area where dispersoids have formed. The accompanying line scan in Fig. 5b (path defined by the red line in Fig. 5a) shows a predictable change in composition from CoCrFeNi-rich dendritic regions to the Cu-rich interdendritic phase. The copper content of the interdendritic phase peaks at around 80 at% Cu. The dendritic phase is deficient in copper relative to the overall alloy composition and enriched in the other four constituents.

Compositional analysis confirms that the intradendritic dispersoids present in the CoCrFeNi-rich dendrite cores are Cu-rich much like the interdendritic Cu-rich phase. Although Fig. 6a suggests that dispersoids present in the dendrite core look morphologically similar, Fig. 6b reveals noticeable compositional differences between dispersoids. The diffuse

Table 2

Trend in atomic percentage of each constituent of drop-tube processed CoCrCuFeNi_{0.8} alloy with droplet diameter in primary dendrites with Cu-rich dispersions (PDD).

	Average Droplet Diameter / μm			
	400	256	181	64
Cr /at %	21.65 \pm 0.06	21.80 \pm 0.22	21.64 \pm 0.19	21.77 \pm 0.09
Fe /at %	20.78 \pm 0.14	20.91 \pm 0.22	20.81 \pm 0.09	21.08 \pm 0.16
Co /at %	20.78 \pm 0.06	20.86 \pm 0.23	21.07 \pm 0.16	20.98 \pm 0.11
Ni /at %	16.44 \pm 0.15	16.32 \pm 0.09	16.56 \pm 0.18	16.44 \pm 0.04
Cu /at %	20.35 \pm 0.34	20.12 \pm 0.51	19.92 \pm 0.29	19.72 \pm 0.34

Table 3

Trend in atomic percentage of each constituent of drop-tube processed CoCrCuFeNi_{0.8} alloy with droplet diameter in primary dendrites without Cu-rich dispersions (PDND).

	Average Droplet Diameter / μm			
	400	256	181	64
Cr /at %	23.84 \pm 1.15	23.13 \pm 1.14	24.39 \pm 0.02	No data
Fe /at %	23.96 \pm 0.10	23.80 \pm 0.13	24.02 \pm 0.02	No data
Co /at %	24.42 \pm 0.48	24.75 \pm 0.50	24.60 \pm 0.24	No data
Ni /at %	17.00 \pm 0.20	16.98 \pm 0.21	16.68 \pm 0.14	No data
Cu /at %	10.78 \pm 0.61	11.34 \pm 0.63	10.32 \pm 0.04	No data

Table 4

Trend in atomic percentage of each constituent of drop-tube processed CoCrCuFeNi_{0.8} alloy with droplet diameter in secondary dendrites without Cu-rich dispersions (SDND) that branch from PDD dendrites.

	Average Droplet Diameter / μm			
	400	256	181	64
Cr /at %	24.53 \pm 0.18	24.36 \pm 0.25	24.26 \pm 0.73	23.77 \pm 0.43
Fe /at %	23.93 \pm 0.34	24.22 \pm 0.29	23.77 \pm 0.38	23.38 \pm 0.55
Co /at %	24.42 \pm 0.26	24.56 \pm 0.36	24.62 \pm 0.78	23.62 \pm 0.46
Ni /at %	16.71 \pm 0.24	16.65 \pm 0.16	16.88 \pm 0.91	16.61 \pm 0.17
Cu /at %	10.40 \pm 0.29	10.21 \pm 0.36	10.46 \pm 0.83	12.63 \pm 1.40

dispersoid (D) possesses a copper composition that hovers around 60 at % with a corresponding depletion in the other constituent elements. The increase in copper across the dispersoid radius is relatively gradual before reaching the maximum in the centre. Conversely, the latter more

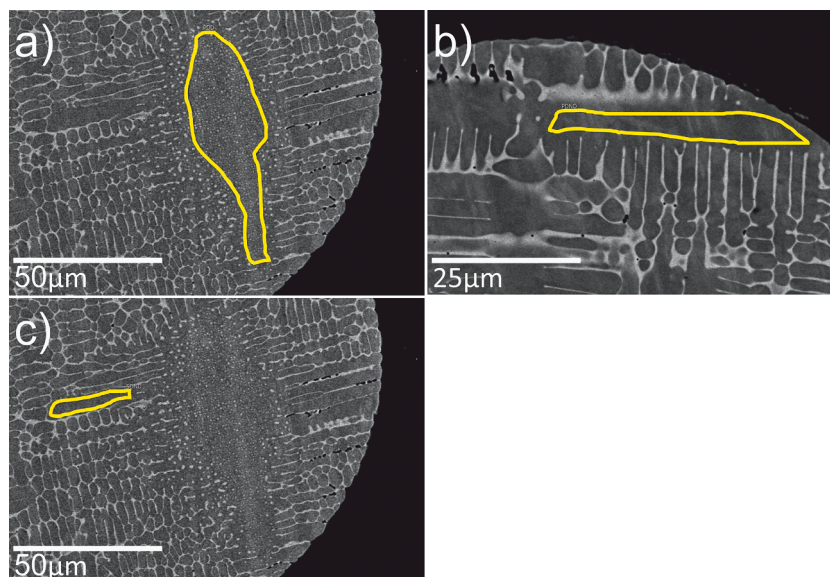


Fig. 4. Examples of EDX mapping of manually defined areas of CoCrCuFeNi_{0.8} droplet microstructures a. primary dendrite with dispersions (PDD) b. primary dendrite with no dispersions (PDND) c. secondary dendrite with no dispersions (SDND) branching from PDD dendrites.

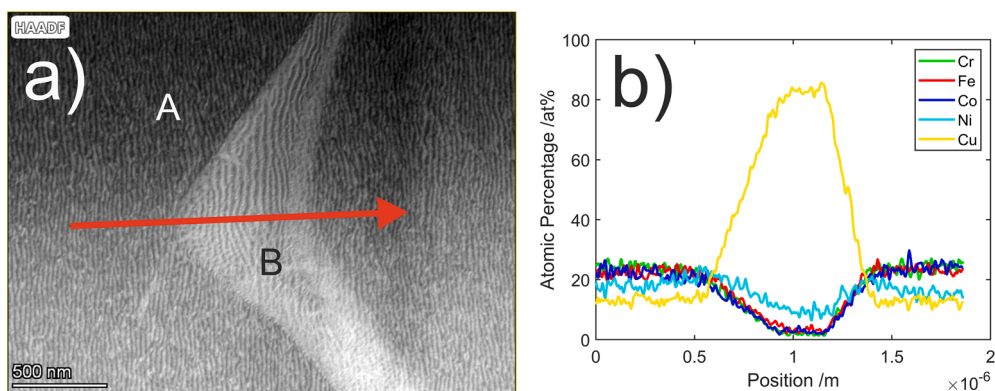


Fig. 5. TEM imaging and compositional analysis of dendritic structure of drop-tube processed CoCrCuFeNi_{0.8} droplet in the 212–150 μm size fraction a. Backscatter imaging of CoCrFeNi-rich dendrites (A) surrounding a Cu-rich interdendritic phase (B) b. EDX line scan showing composition variation of constituent elements across the boundary between the CoCrFeNi-rich dendrites and Cu-rich interdendritic phase.

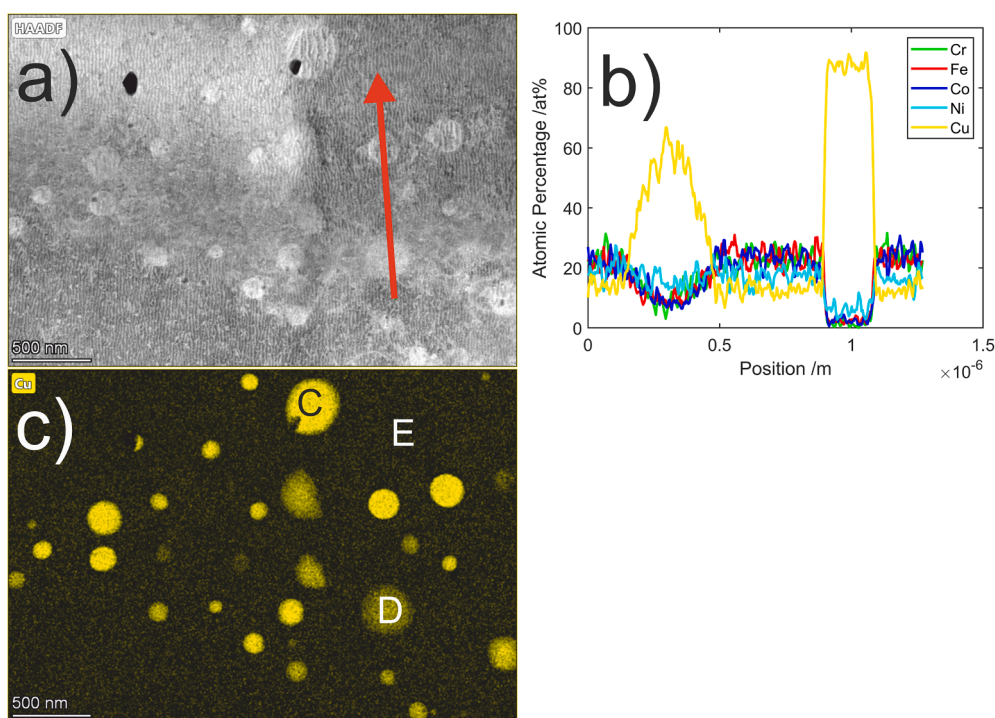


Fig. 6. TEM imaging and compositional analysis of decomposed primary dendrite core of drop-tube processed CoCrCuFeNi_{0.8} droplet in the 212–150 μm size fraction a. Backscatter imaging of dispersoids present in primary dendrite core b. EDX line scan showing composition variation of constituent elements across two Cu-rich dispersoids c. Relative composition (shown in yellow) of copper in well-defined Cu-rich dispersoids (C) and diffuse Cu-rich dispersoids (D) present in a CoCrFeNi-rich matrix (E) in a primary dendrite core of drop-tube processed CoCrCuFeNi_{0.8}.

well-defined dispersoid (C) features a higher copper content of above 80 at% at its centre and a correspondingly larger depletion in the other alloying elements. Furthermore, the transition between CoCrFeNi-rich and Cu-rich phases is much more abrupt at the perceived phase

boundary.

Table 5 shows the result of point-spectra EDX analysis of the various phases in a droplet with dendrites featuring Cu-rich dispersoids. We see that the well-defined Cu-rich dispersoids (C) and the Cu-rich

Table 5

Quantitative composition analysis of phases present in dendritically solidified drop-tube processed CoCrCuFeNi_{0.8} droplets in the 212–150 μm size fraction, and comparison to overall alloy composition and PDD dendrites.

	Alloy	PDD	A	B	C	D	E
Cr /at%	21.6	21.6	24.05 \pm 0.34	1.83 \pm 0.24	1.77 \pm 1.16	8.91 \pm 0.81	23.41 \pm 0.55
Fe /at%	20.7	20.8	23.07 \pm 0.50	3.37 \pm 0.11	2.71 \pm 1.48	9.92 \pm 0.43	22.62 \pm 0.33
Co /at%	20.6	21.1	24.25 \pm 0.93	2.67 \pm 0.39	2.60 \pm 1.27	8.91 \pm 1.28	23.04 \pm 0.27
Ni /at%	16.5	16.6	15.96 \pm 0.83	10.40 \pm 1.38	5.34 \pm 1.58	13.22 \pm 1.74	17.10 \pm 0.40
Cu /at%	20.6	19.9	12.67 \pm 0.14	81.73 \pm 2.12	87.58 \pm 5.46	59.04 \pm 2.79	13.83 \pm 0.34

interdendritic phase (B) possess similar compositions while, correspondingly, the CoCrFeNi-rich dendritic phase between dispersoids in the dendrite core (E) and the dendrites (A) surrounding the Cu-rich interdendritic also possess similar compositions depleted in copper compared to the original alloy and the average composition of the PDD dendrites. The diffuse dispersoids (D) possess compositions that are still heavily Cu-rich, but do not hold as much copper when compared to well-defined dispersoids or the interdendritic phase. While not easily viewable in the backscatter images, the nature of this diffused boundary between the two phases is clearly visible in Fig. 6c, which analyses the Cu-rich dispersions of a dendrite core based on the relative atomic percentage of copper.

The presence of diffuse dispersoids in Fig. 6c could be due to sectioning effects caused by creation of the FIB section prior to analysis in the TEM. If, for example, the apparently spherical dispersoid is sectioned well below or above the equator, we conjecture that the interaction volume of the EDX beam on the TEM could be factoring in the CoCrFeNi-rich phase surrounding (and particularly, below/above) these dispersoids. This would result in the substantially lower copper at %, which would factor in more CoCrFeNi-rich phase surrounding the dispersoids and lower the copper at% reading. This is likely given that the thickness of the FIB section is between 80 and 90 nm, a significant proportion of the size of the dispersoids in the droplet analysed (these range between 25 and 300 nm based on the scale bar in Fig. 6c). Alternatively, the diffuse boundaries could be an indication that the driving force for growth of the Cu-rich dispersoids diminished to zero at an intermediate stage during the formation of certain dispersoids in the dendrite cores. This would indicate that the TEM is capturing Cu-rich precipitates in the middle stages of formation. Whatever the reasoning, we arrive at the same conclusion that the dispersoids with well-delineated boundaries are the likely end-product of the decomposition reaction.

3.7. TEM analysis – phase crystal structure

Fig. 7a and 7b show the locations of the acquired SAED (Selected Area Electron Diffraction) patterns for phase structure analysis in a droplet of drop-tube processed CoCrCuFeNi_{0.8}. The studied area in Fig. 7a is the cross section of a PDD dendrite. Fig. 7c and 7e show the SAED patterns of the analysed phases (Cu-rich dispersoid and CoCrFeNi-rich region between these dispersoids) in Fig. 7a. 7d and 7f denote the SAED patterns of the analysed phases (Cu-rich interdendritic phase and CoCrFeNi-rich dendritic phase) in Fig. 7b. SAED patterns from these four primary phases have been found to be FCC phases. The calculated interplanar spacing of each of the phases present is shown in Table 6. Based on the calculated interplanar spacing we estimate the lattice mismatch between the Cu-rich spherical dispersoids and the CoCrFeNi-rich dendritic phase between the dispersoids (Fig. 7c and 7e respectively) at 0.5 %. This, combined with the fact that both phases consist of an FCC crystal structure, is consistent with the spherical (i.e. non-faceted) morphology of the dispersoids.

4. Discussion

The formation of dispersions within selected dendrite arms creates an additional phase to consider in the microstructure of CoCrCuFeNi_{0.8} compared to droplets which do not feature such dispersoids. We henceforth identify the phases as the CoCrFeNi-rich dendritic phase, the Cu-rich interdendritic, and Cu-rich dispersoids within selected dendrite cores. Given the complexity of the alloy microstructure and the high number of constituent elements, it is difficult to discuss this system in terms of solute partitioning. To simplify the analysis, we treat CoCrCuFeNi_{0.8} as a Cu-HEA pseudobinary, where the HEA phase is CoCrFeNi-rich. When we refer to the ‘solute’ and the associated partition coefficient during solidification or decomposition reactions, we refer largely to copper.

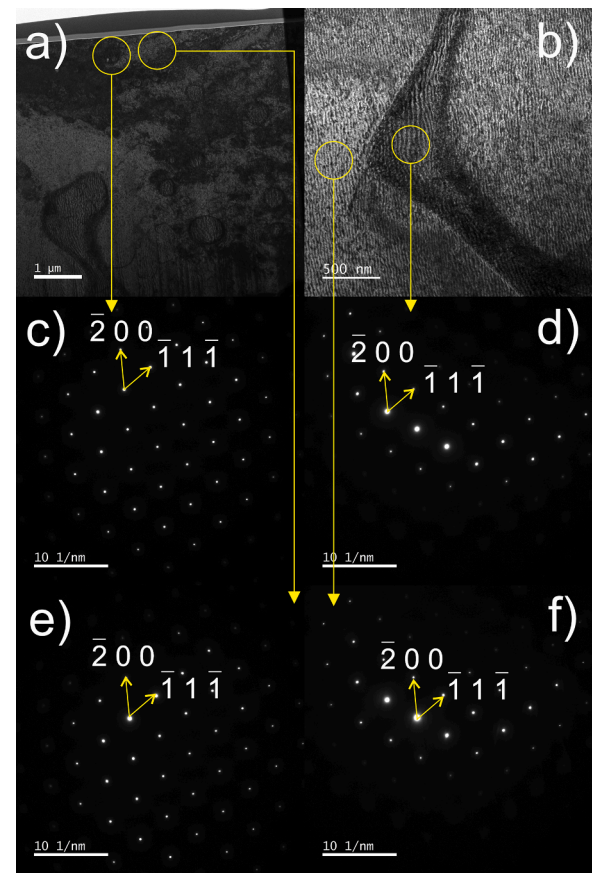


Fig. 7. SAED patterns of primary phases in droplets with dendrites featuring intradendritic Cu-rich dispersoids. a. Example microstructure of dendritic cross-section featuring dispersoids in the core b. Example microstructure of dendritic structure away from areas of dispersoids occurrence c. SAED pattern of Cu-rich dispersoids in dendrite trunk d. SAED pattern of Cu-rich interdendritic phase e. SAED pattern of CoCrFeNi-rich phase between dendritic dispersoids f. SAED pattern of CoCrFeNi-rich dendritic phase far from dispersoids. In all images the zone axis is in the [0 1 1] direction.

Table 6

Crystal structure and interplanar spacing of each principal phase in droplets of CoCrCuFeNi_{0.8} featuring intradendritic dispersoids.

Fig.	Phase	Phase Structure	Interplanar Spacing (Å)
7c	Cu-rich spherical dispersoids	FCC	3.704 ± 4 %
7d	Cu-rich interdendritic	FCC	3.689 ± 4 %
7e	CoCrFeNi-rich between dispersoids	FCC	3.687 ± 4 %
7f	CoCrFeNi-rich dendritic far from dispersoids	FCC	3.666 ± 4 %

Broadly, the dispersoids are Cu-rich, with a similar composition to the Cu-rich interdendritic phase formed during dendritic solidification. The CoCrFeNi-rich phase in the dendrite cores between the dispersoids are correspondingly depleted in copper compared to the average composition of the PDD dendrite core (Table 2). This suggests the dispersoids are the result of a decomposition reaction in these dendrite cores. In line with numerous studies on solidification of copper-containing HEAs, we reason that both the interdendritic phase and the intradendritic dispersoids are highly copper-rich due to preferential rejection of copper, which has a positive enthalpy of mixing with the other alloying elements [18,53–55].

The occurrence of a decomposition reaction means that decomposed regions became supersaturated with copper at some point during the

droplet cooling in freefall. The localisation of these regions in dendrite cores rather than throughout the microstructure supports a decomposition in the solid state after dendrite formation. Three additional phenomena therefore merit explanation:

1. There are prevailing conditions in some dendrite arms that are essential to the occurrence of solid-state decomposition. These conditions are met with more probability in smaller droplets but can also occasionally occur in comparatively large ones.
2. In a specific droplet, these conditions are met with a higher probability in primary dendrites than secondary and tertiary dendrites.
3. In a specific dendrite, whether it be primary, secondary, or tertiary, the conditions are met most regularly in the core of the dendrite arm, rather than on the periphery or the outer edge. More specifically, we note situations such as that represented in Fig. 2d where dispersions in the dendrite cores seem to branch in much the same manner as the dendrites themselves but extend only partially through the solidified dendrite network.

Upon what thermophysical conditions is the occurrence of dendritic dispersions contingent? As this is a rapid solidification study, we first turn our attention to cooling rate and undercooling. In a drop-tube experiment, the cooling rate of the droplet is deterministic whereas the undercooling the liquid droplet reaches before solidification is stochastic. Droplets of similar sizes will experience similar cooling rates but can achieve radically different undercoolings. This is partially due to melt subdivision. Dividing the melt into numerous smaller droplets reduces the likelihood that impurities such as oxides are present in any given droplet to enhance heterogenous nucleation. In general, therefore, dividing the melt into more droplets of lower diameter (and hence, solidifying at a higher prevailing cooling rate) will typically result in a higher undercooling [46,56–58]. By this same logic, a certain small percentage of large droplets can also achieve the undercooling of much smaller droplets. Dispersoid formation that is dependent on undercooling would occur more readily in smaller droplets but could also occasionally occur in the largest droplets produced. This is different from a dependence on cooling rate, where we would expect to see a reduction in occurrence of dispersions to zero at cooling rates below a critical value.

Fig. 3 shows that the percentage of droplets featuring intradendritic dispersions rises almost monotonically with against prevailing cooling rate. However, Cu-rich dispersions are present in all size fractions of drop-tube processed CoCrCuFeNi_{0.8}. This supports a dependence on undercooling rather than cooling rate. Additionally, we observe a large rise in occurrence of dispersions between cooling rates of 2000 K s⁻¹ and 10,000 K s⁻¹. This suggests that a critical undercooling is required to cause the supersaturation of copper that initiates the decomposition reaction following dendritic solidification.

Composition analysis of PDD, PDND and SDND dendrites (Tables 2–4) indicates that a binary set of compositions is created in dendrites of CoCrCuFeNi_{0.8} during solidification. When the dendrites undergo a decomposition reaction after solidification (PDD), the average composition of the decomposed region has been found to match the composition of the original liquid from which the dendrite solidified (i.e. the initial alloy composition). It seems that little or no solute partitioning has taken place in the cores of primary dendrites that have subsequently decomposed. This does not change with droplet size (cooling rate). In stark contrast, primary/secondary undecomposed dendrites (PDND and SDND) are highly depleted in copper and correspondingly enriched in the other constituent elements, displaying clear solute partitioning. Interestingly, the composition of undecomposed primary and secondary dendrites is also constant throughout droplet sizes. Although dendrite growth velocity is dependent on undercooling rather than cooling rate, undercooling is likely to increase with cooling rate as discussed earlier. For this reason, it is unlikely that the partition coefficient has changed extensively even as the degree of undercooling is

likely much higher on average in the smallest droplets than it is for larger ones. Furthermore, the experimental evidence suggests that the change in average composition between undecomposed and decomposed regions within the dendrite arms is best approximated by a step change at the resolutions achievable due to the interaction volume of the EDX detector on the SEM (i.e. within a distance of about 1 μm). This shows that the transition of copper partition coefficient from $k_e \rightarrow 1$ is likely to be abrupt rather than gradual. Such a binary set of compositions being observed despite a continuous rise in cooling rate is therefore difficult to explain using models for kinetic solute trapping such as that postulated by Aziz [19], Aziz and Kaplan [20], Sobolev [28], or Galenko [32]. Were the data to adhere to these models, we would expect to see the average solute (copper) content of decomposed PDD dendrites increasing with increasing prevailing cooling rate and converging towards the composition of copper solute in the initial liquid. Instead, we find a binary set of average dendrite compositions. Dendrites either solidify at the composition of the original liquid, or the equilibrium composition. Fig. 8 shows the approximate correlation of partition coefficient with dimensionless velocity (V/V_{D_b}) in the previously discussed kinetic models as applied to CoCrCuFeNi_{0.8}. For this HEA, we assume a pseudobinary configuration with copper as the solute. An initial equilibrium copper partition coefficient k_e of 0.155 was assumed based on copper concentrations in the dendritic and interdendritic phase following TEM analysis (compositions A and B in Fig. 5). The initial concentration of copper in the liquid at the interface was assumed to be that in the original alloy, $X_0 \cong 1/4.8$. For this example system, the ratio of bulk diffusion to interface diffusion (V_{D_b}/V_{D_i}) is assumed to be 1.25 as proposed by Galenko [32].

As discussed, SEM-derived EDX data in Tables 3 and 4 shows that regardless of cooling rate, composition of CoCrFeNi-rich PDND and SDND dendrites does not change. The superimposed step change shown with a solid black line therefore visually describes the approximate partitioning behaviour we observe in this alloy based on this experimental data. Importantly, the occurrence of the step change from $k_e \rightarrow 1$ at a dimensionless velocity of 1 is purely arbitrary. This transition is likely not due to a critical dendritic growth velocity being reached but rather the result of thermodynamic conditions being met where the alloy liquid is undercooled below T_0 prior to the onset of solidification. This may occur independent of dendrite growth velocity.

Analysis of dendrite growth velocities in compositionally similar alloys also renders the hypothesis of kinetic solute trapping unlikely. Past experiments have noted sluggish dendrite growth velocities

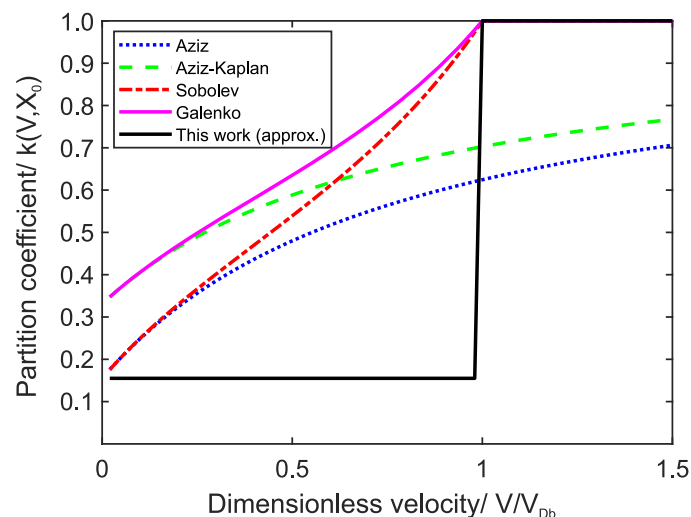


Fig. 8. Comparison of partition coefficient correlation with dimensionless velocity in drop-tube processed CoCrCuFeNi_{0.8} based on experimental data and kinetic models for solute trapping proposed by Aziz [19], Aziz and Kaplan [20], Sobolev [28] and Galenko [32].

attained in solidification studies on multi-component or high-entropy alloys when compared that of binary alloys or intermetallic compounds. Table 7 compares dendritic growth velocity in undercooled samples of equiatomic binary, ternary, quaternary alloys from the Co-Cr-Cu-Fe-Ni family of alloys. Values for dendrite growth velocity in the equiatomic CoCrCuFeNi alloy are also included.

Table 7 indicates a drastic decrease in dendrite growth velocity of up to two orders of magnitude at all undercoolings in quaternary CoCrFeNi and quinary CoCrCuFeNi equiatomic alloys compared to similar binary and ternary alloys. There is argument as to whether the sluggish dendrite growth in this alloy family is due to an increasing number of alloying elements, or due to the specific addition of chromium, which seems to have a profound impact on growth velocity [61]. Andreoli et al. [64] for example, found growth velocities in quaternary CoCrFeNi that were comparable to similar ternary alloys rather than the much lower velocities Wang et al. [63] calculate for the same alloy. Regardless, because CoCrCuFeNi_{0.8} has both a high number of constituent elements and a significant chromium content, we reason that dendrite growth would be both similar to that of equiatomic CoCrCuFeNi and considerably slower than that in binary alloys. Significant kinetic solute trapping is contingent on dendrite growth velocity being on par with solute diffusion velocity across the solid liquid interface. It seems, therefore, that growth conditions in CoCrCuFeNi_{0.8} do not encourage solute trapping even at high undercoolings achievable during drop-tube processing.

The kinetic models discussed above are therefore not applicable to the majority of our results. We suggest, therefore, that the complete solute trapping that occurs in these dendrites is not due to a kinetic effect, but a thermodynamic one. The key requirement is that the temperature of the growing dendrites is below the T_0 temperature of the alloy at the chosen composition.

In line with similar arguments such as those presented in [33–39] for conventional alloys and [40–43] in HEAs, we believe partitionless solidification is occurring in CoCrCuFeNi_{0.8} above a critical undercooling ΔT^* defined by Eckler et al. [27]. Above such an undercooling, the temperature of the alloy is decreased below the T_0 line of the phase diagram, making partitionless solidification thermodynamically possible [25]. If cooled below T_0 at the onset of solidification, the growing dendrite will initially possess a composition that is the same as the composition of the parent liquid and, hence, the composition of the alloy itself. The partition coefficient would therefore be $k = 1$. Because the partitionless solidification is not dependent on cooling rate, dendrites in a droplet of any size can solidify in this way as long as they are undercooled below T_0 . All PDD dendrite cores will therefore have an average composition equal to the original liquid regardless of the cooling rate at which they were solidified. This is confirmed experimentally in Table 2.

Once nucleated solid dendrites begin to grow however, latent heat is released continuously into the interdendritic liquid, raising the temperature at the interface between the two phases. As the temperature of the residual liquid continues to increase, there comes a point where the undercooling would decrease below ΔT^* . Temperature at the interface

correspondingly increases back above T_0 . Above this temperature, partitionless solidification can no longer take place and partitioning begins. Any solid growing and coarsening from this point forward would have a composition distinct from the initial liquid. This is supported by the compositional data in Tables 3 and 4, where PDND and SDND dendrites, that have not undergone decomposition, are substantially depleted in copper compared to starting alloy. This copper has partitioned to the interdendritic phase.

The thermodynamic argument also seems sound when we consider the occurrence of dispersoids overwhelmingly in the primary dendrites. During dendritic solidification, the primary dendrite trunk will always begin to form before secondary and tertiary branching begins. It is more likely that the primary dendrite, which formed first, grew into a melt undercooled below ΔT^* . Within one dendrite arm, the same reasoning can be used to explain why partitioning is only present in dendrite cores (i.e. the areas of the dendrite arm that solidified first). The edges of the dendrite, and the region of the dendrite interior immediately adjacent, are closer to the interface between the growing dendrite and the interdendritic liquid than the areas near the core of the dendrite. The change in morphology between the dendrite core and the outer edges of the dendrite visually represents the point in dendrite growth and coarsening at which the rise in temperature at the solid-liquid interface brought on a change from partitionless solidification to conventional partitioning of the solute. The extent to which dispersoids are present in dendrites is therefore clearly contingent on undercooling. This is demonstrated by the increasing volume fraction occupied by dispersoids in droplets that have undergone partitionless solidification (see Fig. 3). As cooling rate rises, a given droplet (on average) is undercooled further below T_0 for the given composition. A comparatively higher amount of energy in the form of latent heat is required to be released to raise the temperature of the remaining liquid back above T_0 for solute partitioning to resume during the remaining solidification process. Zones of the droplet which solidified in a partitionless manner would therefore occupy a more significant volume fraction of the droplet in question.

In the undecomposed dendrites, the lack of a substantial composition change with cooling rate is understandable when we consider the sluggish dendritic growth in this alloy compared to many binary alloys. Kinetic models relating dendrite growth velocity to partition coefficient now become more applicable. When solidification is no longer partitionless, the presumed low dendrite growth velocity in this alloy, even at high undercoolings (Table 7), will kinetically limit the changes in partition coefficient k . The coefficient will hence always remain near k_e until undercooling reaches the critical value ΔT^* . Once this critical undercooling is exceeded, the equilibrium constant will tend towards unity ($k \approx 1$).

With the experimental data supporting a transition to partitionless solidification in CoCrCuFeNi_{0.8} at high undercoolings, we expect a shift from growth controlled by solute diffusion to growth controlled by the diffusion of heat as is commonly encountered in pure metals. Such a change in growth mechanism generally results in a massive rise in dendrite growth velocity. This transition has been suggested to occur in equiatomic CoCrCuFeNi by Yan et al. [45]. However, it is intriguing that past glass fluxing and electromagnetic levitation (EML) experiments on similar alloys in the Co-Cr-Cu-Fe-Ni family have not observed instances of solid state dispersoids forming within the solidified dendrite trunks during the transition from solute to thermally controlled growth [18,63, 65–68]. We suggest that the supersaturation is avoided due to the ability of the equiatomic alloy (and many of its studied compositional variations) to undergo liquid phase separation (LPS) in the metastable regime upon deep undercooling. If the alloy has already undergone a phase separation prior to solidification, likely into a Cu-rich and CoCrFeNi-rich liquid, the copper solute content of a subsequent CoCrFeNi-rich solidifying dendritic phase would be lower than that of the starting alloy, even if it solidified in a partitionless manner. We posit that this would reduce the effect of any solute trapping and avoid copper supersaturation.

Why does LPS not seem to occur in CoCrCuFeNi_{0.8} during non-

Table 7

Dendrite growth velocities in equiatomic Co-Cr-Cu-Fe-Ni family alloys with increasing liquid phase undercooling, calculated from fit equation or estimated visually based on graphical data.

Alloy	$V_{(\Delta T=50\text{ K})}$	$V_{(\Delta T=100\text{ K})}$	$V_{(\Delta T=200\text{ K})}$	Source
CoFe	~1	~5	~20	[59]
CoNi	~4	~15	~50	[60,61]
CoFeNi	~4	~15	~35	[61]
CuFeNi	2.9	8.1	22.6	[62]
CoCrFeNi	0.0001	0.006	0.36	[63]
CoCrCuFeNi	0.02	0.12	0.81	[63]
	0.02	0.15	1	[18]
	0.02	0.27	3.51	[45]

equilibrium processing? One possible explanation lies in the composition. Although the CoCrCuFeNi_{0.8} alloy element ratio was chosen to enhance the likelihood of LPS at lower undercoolings, the composition difference may have affected the solidification pathway in an unpredictable manner. The lack of fully accurate phase diagrams for this multicomponent alloy system makes this difficult to verify. The depletion in nickel and slight enhancement of chromium content of about 2 at % (due to the nature of the alloy production process) may have removed the possibility of LPS in the alloy entirely or raised the critical undercooling to a value difficult to achieve in the drop-tube. This would be unusual, however, given that lowering of nickel and raising of chromium content have been shown to enhance the initiation of LPS in transition metal based HEAs [54].

Another explanation for the lack of LPS in the alloy is based on the fundamental difference between undercooling experimental methods such as EML and glass fluxing, and the rapid quenching study presented here. In the drop-tube, high undercooling is achieved, in part, through the high cooling rate in the ejected liquid, rather than solely through the inhibition of heterogenous nucleation. Glass fluxing and EML experiments hold the liquid in the undercooled state on a timescale that is orders of magnitude longer than in drop-tube experiments [56,69]. At induced cooling rates of up to 60,000 K s⁻¹ estimated in our experiment, binodal LPS may have been suppressed in drop-tube processed CoCrCuFeNi_{0.8}. Such a phenomenon has previously been observed by Xia et al. [70] in a drop-tube study of ternary Fe_{62.5}Cu_{27.5}Sn₁₀ alloy. LPS structures at intermediate cooling rates gave way to equiaxed dendrites in the quickest cooling droplets.

It is notable that a multicomponent alloy such as this did not form a bulk metallic glass upon solidification at high cooling rates. Although the addition of more elements into the melt is thought to enhance the possibility of glass formation [71]. Inoue posits that a negative enthalpy of mixing and a large atomic size difference between the three primary components are also necessary to suppress crystal growth and raise the glass transition temperature to a more accessible value [72]. CoCrCuFeNi_{0.8} possesses a positive mixing enthalpy of 3.70 kJ mol⁻¹ (calculated from theoretical data in [73]) and an atomic size difference of 1.05 % (calculated using data in [74]). Glass formation is therefore unlikely for this alloy.

From this investigation we suggest a few conditions that may favour partitionless solidification in HEAs.

1. The alloy is undercooled below the T_0 temperature for the given composition
2. Dendrite growth velocity is sluggish compared to diffusion of solute across solid-liquid interface – even at relatively high undercoolings
3. Enthalpy of mixing is not highly negative (to avoid the formation of metallic glass during rapid solidification)
4. Low atomic size difference (to avoid the formation of metallic glass during rapid solidification)
5. Inhibition of LPS via rapid cooling

Having established that dendrites with Cu-rich dispersoids present are the result of partitionless solidification, we must next discuss the phase transformation that causes the formation of such dispersoids. Because a decomposition reaction is occurring in the solid state, a miscibility gap is likely present in the alloy phase diagram below the liquidus temperature. Thermodynamic data seems to substantiate this claim. Using values from the SG SOL solutions database version 4.42, compiled by Scientific Group Thermodata Europe (SGTE), we have determined the interaction parameters between each binary pair present in CoCrCuFeNi_{0.8} for an FCC solid solution phase (chosen because the solidified microstructure seems to consist exclusively of FCC phases). Considering the pseudo-binary system CoCrFeNi_{0.8}-Cu, we have evaluated the Gibbs free energy curve of an FCC phase across the composition range at various temperatures. This is determined through the CALPHAD methodology defined in [75,76]. At various temperatures

below the liquidus, we use the common tangent method to pinpoint two compositions on the free energy curve from which the binode can be defined. Inflection points in the free energy curve (i.e. where the second derivative is equal to zero), are also found for each temperature across a defined range, with each temperature corresponding to two additional distinct compositions. The curve delineated by these composition values is the chemical spinode. For solid CoCrCuFeNi_{0.8} with a FCC crystal structure, the estimated binodal and spinodal curves are shown in Fig. 9. A more detailed explanation about how the curves were constructed is given in the supplementary information (Online Resource 3).

As shown in Fig. 9, a miscibility gap is indeed predicted across a large part of the composition range. The binode curve (solid black) and spinode curve (dot-dashed black) are plotted below the liquidus (solid blue). At the initial alloy composition, the atomic ratio of copper is 0.208. Below the liquidus, the interval between the binode and spinode defines a temperature interval from 1648 K and 1361 K where phase separation can occur via a nucleation and growth mechanism. Below 1361 K, it is predicted that the phase separation will instead proceed via spinodal decomposition. Of these two possibilities, the mechanism which occurred in this experiment merits further discussion.

One key initial consideration must first be remembered. The calculated miscibility gap in Fig. 9 represents a solid-state miscibility gap in an FCC phase at the starting alloy composition. In other words, the precursor phase is an FCC phase that has solidified in a partitionless manner from the liquid alloy and thus, has the same initial composition as the original alloy. If T_0 were found to be below 1361 K, i.e. the temperature below which spinodal decomposition is predicted to occur at the original alloy composition, phase separation by nucleation and growth between the binode and spinode would be impossible. Such work is impossible in the drop-tube but may be achievable in EML experiments.

One argument pointing to a nucleation and growth mechanism is the large size distribution in the Cu-rich dispersoids, even within only one dendrite core. This is visualised in Fig. 6c where dispersoids in the pictured dendrite core range from <50 nm to over 300 nm in diameter, a spread across almost an order of magnitude. Furthermore, Fig. 6d shows that, at least in well-defined dispersoids (i.e. those unaffected by sectioning during preparation of the TEM FIB sample), there is an extremely well-defined interface between the dispersoid and the CoCrFeNi-rich phase which surrounds it. Finally, the isolated sphere morphology of the dispersoids is also characteristic of a nucleation and growth reaction [77]. Because of the large number density of these dispersoids in the dendrite cores, copious nucleation would need to occur throughout the regions that had undergone partitionless solidification, this renders this explanation more unlikely, but not impossible. Particularly during rapid cooling, initial solidification may cause the retention of dislocations and vacancies within a phase down to low temperatures. Along with other impurities (e.g. oxides), these vacancies and dislocations provide favourable sites for heterogenous nucleation of precipitate phases in the solid state. It is conceivable that the prevalence of such impurities has caused the copious nucleation of the observed Cu-rich dispersoids in the dendrite cores [78].

The key argument for a spinodal decomposition mechanism is the inability to suppress the formation of the Cu-rich dispersoids, even at predicted solid-phase cooling rates of up to 40,000 K s⁻¹. Experiments in rapid cooling of other HEAs have revealed similar unavoidable decomposition. Singh et al. [11] observed spinodal decomposition in the dendritic phase in the as-cast sample of AlCoCrCuFeNi, yielding interconnected B2 phase precipitates aligned preferentially along $\langle 110 \rangle$ directions. Importantly, they also observed grains of a sample splat quenched at cooling rates of 10⁶ – 10⁷ K s⁻¹ which featured nanoscale ordered BCC domains, indicating that a decomposition reaction occurs even at high cooling rates. This was reaffirmed by Zhang et al. [79] who cooled the same alloy via melt-spinning and spray casting, achieving similarly high cooling rates. A clear spinodal microstructure is observed in the solidified dendritic phase, with a B2 phase network aligned along

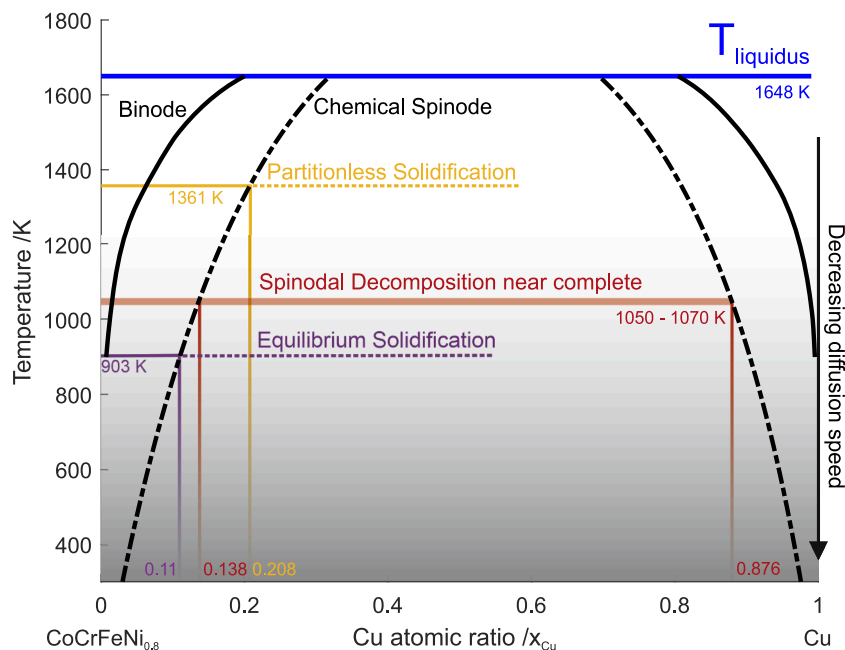


Fig. 9. Plotted binode and spinode in solid FCC phase of CoCrCuFeNi_{0.8} based on thermochemical data in the SGsol solutions database version 4.42, compiled by SGTE.

the same $\langle 1\ 1\ 0 \rangle$ directions.

In contrast to these studies, the morphology of the precipitated phase in CoCrCuFeNi_{0.8} is drastically different from what would be considered a conventional spinodal decomposition structure in an alloy. Instead of the interconnected network structure, we find discrete spheres of the precipitated phase. It is therefore important to note that in a two-phase system with a large mismatch between volume fraction of the phases, the spinodal decomposition microstructure may also appear in the form of discrete dispersoids rather than the interconnected or percolated network typically expected [80]. Cahn suggests that a minimum volume fraction of each phase of around 15 % may be necessary [81]. In the decomposed regions in the dendrites of CoCrCuFeNi_{0.8}, the volume fraction occupied by the Cu-rich dispersoid phase is very low, perhaps about 10 %. This suggests that not enough Cu-rich phase is formed during the decomposition process for a network structure to percolate. In lieu of this, a discrete island structure is created [82–84].

The final shape of precipitated phases is equally complex to determine. Generally, differences in the crystal structure and/or interplanar spacings in the coexisting phases will introduce a certain amount of misfit strains into the crystal lattice around the precipitate(s) [80]. Low lattice misfit strain and a balanced volume fraction will likely result in the well-known random interconnected network structure [81]. A lattice misfit too far over 0.5 % is likely to cause a change in shape of the precipitated phase from spherical to faceted shapes such as plates or cubes as precipitates grow along preferred directions due to elastic anisotropies [80,85,86]. Examples of spinodal decomposition morphologies growing along preferred crystallographic directions are modelled in the work of Nishimori et al. [84] and visible in the work on AlCoCrCuFeNi discussed above [11,79]. Because all of the principal phases in the decomposed dendrites of the CoCrCuFeNi_{0.8} have been found to have a FCC phase structure and a very similar interplanar spacing, lattice mismatch between the phases is about 0.5 % and elastic forces are likely isotropic. This means that any combination of these two phases would likely form a non-faceted phase boundary. In this case, a spherical interface forms preferentially to minimise interface energy [78].

Unfortunately, it is extremely difficult to definitively state whether these dispersoids are the result of nucleation and growth or spinodal decomposition reactions. For this, specific high-resolution analysis

techniques are required to capture the initial stages of the decomposition reaction at the nanoscale. Much of these techniques involve the observation of increasing amplitude of composition modulations of the precipitating phase with aging time in samples which have been deeply quenched into the unstable region of the miscibility gap (i.e. below the spinode). The resolution of these modulations may be on the order of 1 nm [77]. Such a composition increase with aging time was conclusively shown in during aging of Fe-29at% Cr-14at% Co-21at% Al-0.15at% Zr by Zhu et al. [87] using a combination of Field Ion Microscopy (FIM) and Atomic Force Probing (AFP), proving a spinodal decomposition had occurred. More recently, various other methods have been used to study spinodal reactions [88], however, such experiments are out of the scope of this work. On balance, we believe that it is more likely that a spinodal decomposition reaction in the dendrite cores is the precursor to the final observed microstructure, primarily because of the inability to suppress the reaction at extremely high cooling rates.

The final compositions of the Cu-rich and CoCrFeNi-rich phases in the decomposed dendrite arms (compositions C and E in Table 5) correspond to a temperature of 1060 – 1070 K based on the plotted spinodal curve. This temperature therefore likely represents the alloy composition after spinodal decomposition and subsequent coarsening. This coarsening is a diffusion process confined to a time window between the onset of the spinodal reaction and the kinetic inhibition of coarsening due to the rapidly dropping temperature.

Conventionally, we treat substitutional diffusion in a crystalline solid as significant until the temperature falls to a value between $0.7T_L$ and $0.5T_L$ where T_L is the liquidus temperature [89,90]. Taking an intermediate value of $0.6T_L$ in CoCrCuFeNi_{0.8} corresponds to a temperature of 990 K. We can therefore predict a change in the ability of the spinodal decomposition reaction to progress based on the starting composition of the dendrites formed immediately after solidification. In the first scenario, we assume partitionless solidification and hence use the overall alloy composition CoCrCuFeNi_{0.8} as the starting dendrite composition, where the atomic ratio of copper is 0.208. For the other scenario we use the copper composition of a dendrite in a droplet where equilibrium partitioning occurred during solidification (0.11, an average composition of undecomposed CoCrFeNi-rich dendrites). By plotting these values on the x-axis of Fig. 9 and finding the corresponding temperature on the spinodal curve, we see that in dendrites that solidified in a

partitionless manner, the spinodal decomposition temperature is about 1361 K. In contrast, in a dendrite that solidified under equilibrium partitioning conditions, the spinode is intersected at 903 K. In the first case, the spinodal reaction occurs at a temperature well above the proposed limit of 990 K. Solid state diffusion would be significant, and the kinetics are favourable for a spinodal reaction and subsequent coarsening to proceed. However, where the dendrite has solidified under equilibrium conditions, the temperature at which spinodal decomposition occurs is below that at which diffusion would likely become significantly kinetically hindered. We posit, therefore, that the spinodal decomposition reaction and formation of Cu-rich dispersoids is only kinetically viable in dendrites that have solidified in a partitionless manner from the melt. This analysis, while tentative due to the lack of complete thermodynamic data to describe multicomponent systems, strengthens the argument for spinodal decomposition and further explains the selective occurrence of these dispersions in dendrites that have undergone partitionless solidification.

5. Conclusion

Thorough microstructural investigation has been undertaken on rapidly solidified CoCrCuFeNi_{0.8} droplets cooled at rates between 600 K s⁻¹ and 60,000 K s⁻¹. We find that the presence of Cu-rich dispersoids in the cores of CoCrFeNi-rich dendrite arms of some droplets is due to partitionless solidification of an initial dendritic phase followed by spinodal decomposition within the dendrite arms where solidification in this manner occurred. The cores of dendrites containing dispersoids were found to have the same average composition as the overall alloy. This, and the lack of any change in average composition of decomposed primary dendrites across all droplet sizes, points towards partitionless solidification dependent more on thermodynamic conditions rather than reaction kinetics. A critical undercooling is required for partitionless solidification to occur, and cooling rate is important only insofar as it generally causes an increase in prevailing undercooling.

Data availability

Raw data collected for the purposes of this investigation will be made available via the White Rose Repository (<https://eprints.whiterose.ac.uk>) upon final acceptance of this manuscript

CRediT authorship contribution statement

L.S.E. Teggin: Writing – original draft, Visualization, Validation, Software, Methodology, Investigation, Formal analysis, Data curation, Conceptualization. **R.F. Cochrane:** Writing – review & editing, Supervision, Methodology, Formal analysis, Conceptualization. **S.L. Mick-lethwaite:** Investigation. **Z.P. Aslam:** Investigation. **A.E. Nassar:** Investigation. **A.M. Mullis:** Writing – review & editing, Supervision, Software, Methodology, Formal analysis, Conceptualization.

Declaration of competing interest

The authors declare that they have no known competing financial interests or personal relationships that could have appeared to influence the work reported in this paper.

Acknowledgements

This work was supported by an Engineering and Physical Sciences Research Council (EPSRC) Doctoral Training Partnership (DTP) Scholarship.

Supplementary materials

Supplementary material associated with this article can be found, in

the online version, at [doi:10.1016/j.actamat.2025.120858](https://doi.org/10.1016/j.actamat.2025.120858).

References

- [1] F. Otto, A. Dlouhý, K.G. Pradeep, M. Kuběnová, D. Raabe, G. Eggeler, E.P. George, Decomposition of the single-phase high-entropy alloy CrMnFeCoNi after prolonged anneals at intermediate temperatures, *Acta Mater.* 112 (2016) 40–52.
- [2] B. Schuh, B. Völker, J. Todt, N. Schell, L. Perrière, J. Li, J. Couzinié, A. Hohenwarter, Thermodynamic instability of a nanocrystalline, single-phase TiZrNbHfTa alloy and its impact on the mechanical properties, *Acta Mater.* 142 (2018) 201–212.
- [3] N.Y. Yurchenko, N.D. Stepanov, M.A. Tikhonovsky, G.A. Salishchev, Phase evolution of the Al x NbTiVZr (x = 0; 0.5; 1; 1.5) high entropy alloys, *Metals (Basel)* 6 (12) (2016) 298.
- [4] N.Y. Yurchenko, N. Stepanov, A. Gridneva, M. Mishunin, G. Salishchev, S. Zherebtsov, Effect of Cr and Zr on phase stability of refractory Al-Cr-Nb-Ti-V-Zr high-entropy alloys, *J. Alloys. Compd.* 757 (2018) 403–414.
- [5] F. Thiel, D. Geissler, K. Nielsch, A. Kauffmann, S. Seils, M. Heilmaier, D. Utt, K. Albe, M. Motylenko, D. Rafaja, Origins of strength and plasticity in the precious metal based high-entropy alloy AuCuNiPdPt, *Acta Mater.* 185 (2020) 400–411.
- [6] S. Drescher, S. Seils, D. Pohl, B. Rellinghaus, A. Kauffmann, M. Heilmaier, J. Freudenberger, Softening by spinodal decomposition in Au-Cu-Ni-Pd-Pt high-entropy alloys, *Mater. Sci. Eng.: A* 887 (2023) 145772.
- [7] A. Munitz, L. Meshi, M. Kaufman, Heat treatments' effects on the microstructure and mechanical properties of an equiatomic Al-Cr-Fe-Mn-Ni high entropy alloy, *Mater. Sci. Eng.: A* 689 (2017) 384–394.
- [8] Y. Wang, B. Li, M. Ren, C. Yang, H. Fu, Microstructure and compressive properties of AlCrFeCoNi high entropy alloy, *Mater. Sci. Eng.: A* 491 (1–2) (2008) 154–158.
- [9] A. Manzoni, H. Daoud, R. Völkl, U. Glatzel, N. Wanderka, Phase separation in equiatomic AlCoCrFeNi high-entropy alloy, *Ultramicroscopy*. 132 (2013) 212–215.
- [10] E. Pickering, H. Stone, N. Jones, Fine-scale precipitation in the high-entropy alloy Al_{0.5}CrFeCoNiCu, *Mater. Sci. Eng.: A* 645 (2015) 65–71.
- [11] S. Singh, N. Wanderka, B. Murty, U. Glatzel, J. Banhart, Decomposition in multi-component AlCoCrCuFeNi high-entropy alloy, *Acta Mater.* 59 (1) (2011) 182–190.
- [12] G. Colligan, B. Bayles, Dendrite growth velocity in undercooled nickel melts, *Acta Metallurgica* 10 (9) (1962) 895–897.
- [13] S. Battersby, R. Cochrane, A. Mullis, Growth velocity-undercooling relationships and microstructural evolution in undercooled Ge and dilute Ge-Fe alloys, *J. Mater. Sci.* 34 (1999) 2049–2056.
- [14] S. Luo, W. Wang, J. Chang, Z. Xia, B. Wei, A comparative study of dendritic growth within undercooled liquid pure Fe and Fe₅₀Cu₅₀ alloy, *Acta Mater.* 69 (2014) 355–364.
- [15] O. Funke, G. Phanikumar, P. Galenko, L. Chernova, S. Reutzel, M. Kolbe, D. Herlach, Dendrite growth velocity in levitated undercooled nickel melts, *J. Cryst. Growth* 297 (1) (2006) 211–222.
- [16] D.M. Herlach, Dendrite growth kinetics in undercooled melts of intermetallic compounds, *Crystals (Basel)* 5 (3) (2015) 355–375.
- [17] D.M. Herlach, Solidification from undercooled melts, *Mater. Sci. Eng.: A* 226 (1997) 348–356.
- [18] W. Wang, L. Hu, S. Luo, L. Meng, D. Geng, B. Wei, Liquid phase separation and rapid dendritic growth of high-entropy CoCrCuFeNi alloy, *Intermetallics (Barking)* 77 (2016) 41–45.
- [19] M.J. Aziz, Model for solute redistribution during rapid solidification, *J. Appl. Phys.* 53 (2) (1982) 1158–1168.
- [20] M.J. Aziz, T. Kaplan, Continuous growth model for interface motion during alloy solidification, *Acta Metallurgica* 36 (8) (1988) 2335–2347.
- [21] P.M. Smith, M.J. Aziz, Solute trapping in aluminum alloys, *Acta Metallurg. et materialia* 42 (10) (1994) 3515–3525.
- [22] J. Kittl, P. Sanders, M. Aziz, D. Brunco, M. Thompson, Complete experimental test of kinetic models for rapid alloy solidification, *Acta Mater.* 48 (20) (2000) 4797–4811.
- [23] J.A. Kittl, M. Aziz, D.P. Brunco, M. Thompson, Nonequilibrium partitioning during rapid solidification of Si-As alloys, *J. Cryst. Growth* 148 (1–2) (1995) 172–182.
- [24] W. Kurz, D. Fisher, *Fundamentals of Solidification*, Trans Tech Publications Limited, 1998.
- [25] J. Baker, J. Cahn, *Solidification*, American Society for Metals, Metals Park, OH, 1971, p. 23.
- [26] R. Willnecker, D. Herlach, B. Feuerbacher, Evidence of nonequilibrium processes in rapid solidification of undercooled metals, *Phys. Rev. Lett.* 62 (23) (1989) 2707.
- [27] K. Eckler, R. Cochrane, D. Herlach, B. Feuerbacher, M. Jurisch, Evidence for a transition from diffusion-controlled to thermally controlled solidification in metallic alloys, *Phys. Rev. B* 45 (9) (1992) 5019.
- [28] S. Sobolev, Local non-equilibrium diffusion model for solute trapping during rapid solidification, *Acta Mater.* 60 (6–7) (2012) 2711–2718.
- [29] S. Sobolev, Local-nonequilibrium model for rapid solidification of undercooled melts, *Phys. Lett. A* 199 (5–6) (1995) 383–386.
- [30] S. Sobolev, Effects of local non-equilibrium solute diffusion on rapid solidification of alloys, *Phys. Status Solidi (a)* 156 (2) (1996) 293–303.
- [31] S. Sobolev, On the transition from diffusion-limited to kinetic-limited regimes of alloy solidification, *Acta Mater.* 61 (20) (2013) 7881–7888.
- [32] P. Galenko, Solute trapping and diffusionless solidification in a binary system, *Phys. Rev. E* 76 (3) (2007) 031606.
- [33] B. Cantor, W. Kim, B. Bewlay, A. Gillen, Microstructure—cooling rate correlations in melt-spun alloys, *J. Mater. Sci.* 26 (1991) 1266–1276.

- [34] J.T. McKeown, L.L. Hsiung, H.J. Ryu, J.M. Park, P.E. Turchi, W.E. King, Rapidly solidified U-6 wt% Nb powders for dispersion-type nuclear fuels, *J. Nuclear Mater.* 448 (1–3) (2014) 72–79.
- [35] J.T. McKeown, L.L. Hsiung, J.M. Park, H.J. Ryu, P.E. Turchi, W.E. King, Size-dependent microstructures in rapidly solidified uraniumniobium powder particles, *J. Nuclear Mater.* 479 (2016) 1–10.
- [36] O.V. Gusakova, P.K. Galenko, V.G. Shepelevich, D.V. Alexandrov, M. Rettenmayr, Diffusionless (chemically partitionless) crystallization and subsequent decomposition of supersaturated solid solutions in Sn–Bi eutectic alloy, *Philosoph. Trans. R. Soc. A* 377 (2143) (2019) 20180204.
- [37] M.R. Abul, R.F. Cochrane, A.M. Mullis, Partitionless solidification and anomalous triradial crystal formation in drop-tube processed Al-3.9 wt% Fe alloys, *Mater. Today Commun.* 31 (2022) 103274.
- [38] M.R. Abul, R.F. Cochrane, A.M. Mullis, A. Nassar, Microstructural evolution and mechanical properties of drop tube processed Al-4.1 wt.% Fe-1.9 wt.% Si, *J. Mater. Eng. Perform.* (2023) 1–17.
- [39] O. Gusakova, Chemically partitionless crystallization in near-eutectic rapidly solidified Al–12, 6Si–0, 8Mg–0, 4Mn–0, 7Fe–0, 9Ni–1, 8Cu alloy, *Eur. Phys. J. Special Topics* (2023) 1–11.
- [40] B. Vishwanadh, N. Sarkar, S. Gangil, S. Singh, R. Tewari, G. Dey, S. Banerjee, Synthesis and microstructural characterization of a novel multicomponent equiatomic ZrNbAlTiV high entropy alloy, *Scr. Mater.* 124 (2016) 146–150.
- [41] E. Ananiadis, K. Lentzaris, E. Georgatis, C. Mathiou, A. Poulia, A. Karantzalis, AlNiCrFeMn equiatomic high entropy alloy: a further insight in its microstructural evolution, mechanical and surface degradation response, *Met. Mater. Int.* 26 (2020) 793–811.
- [42] C. Mathiou, D. Ganara, E. Georgatis, A. Poulia, K. Lentzaris, A. Karantzalis, Adjustment of hardness of (CrFeMn)_x(Ni y Al)_{1-x} (y= 1, 3 and x= 0.6, 0.72, 0.80) high entropy alloys by deliberate control of intermetallic phase formation: microstructural evolution, hardness and dry-sliding wear response, *Met. Mater. Int.* 27 (2021) 175–192.
- [43] K. Srimark, S. Dasari, A. Sharma, P. Wangyao, B. Gwalani, T. Rojhirunsakool, S. Gorsse, R. Banerjee, Hierarchical phase evolution in a lamellar Al_{0.7}CoCrFeNi high entropy alloy involving competing metastable and stable phases, *Scr. Mater.* 204 (2021) 114137.
- [44] K. Bai, C.K. Ng, M. Lin, B. Cheng, Y. Zeng, D. Wu, J.J. Lee, S.L. Teo, S.R. Ng, D.C. C. Tan, Unexpected spinodal decomposition in as-cast eutectic high entropy alloy Al₃₀Co₁₀Cr₃₀Fe₁₅Ni₁₅, *Mater. Des.* 236 (2023) 112508.
- [45] P. Yan, J. Chang, W. Wang, X. Zhu, M. Lin, B. Wei, Metastable phase separation and crystalline orientation feature of electromagnetic levitation processed CoCrCuFeNi high entropy alloy, *Acta Mater.* (2024) 119778.
- [46] O. Oloyede, T.D. Bigg, R.F. Cochrane, A.M. Mullis, Microstructure evolution and mechanical properties of drop-tube processed, rapidly solidified grey cast iron, *Mater. Sci. Eng.: A* 654 (2016) 143–150.
- [47] O.E. Jegede, R.F. Cochrane, A.M. Mullis, Metastable monotectic phase separation in Co–Cu alloys, *J. Mater. Sci.* 53 (16) (2018) 11749–11764.
- [48] X. Liu, X. Lu, B. Wei, Rapid monotectic solidification under free fall condition, *Sci. China Series E: Technol. Sci.* 47 (2004) 409–420.
- [49] L.S.E. Teggin, R.F. Cochrane, A.M. Mullis, Characterisation of phase separation in drop-tube-processed rapidly solidified CoCrCuFeNi_{0.8} high-entropy alloy, *High Entropy Alloys Mater.* (2024).
- [50] E.A. Brandes, G. Brook, *Smithells Metals Reference Book*, Elsevier, 2013.
- [51] Bonnell, D., Treverton, J., Valerga, A. and Margrave, J. *The emissivities of liquid metals at their fusion temperatures*. 1972.
- [52] E.-S. Lee, S. Ahn, Solidification progress and heat transfer analysis of gas-atomized alloy droplets during spray forming, *Acta Metallurgica et Materialia* 42 (9) (1994) 3231–3243.
- [53] N. Derimow, R. Abbaschian, Liquid phase separation in high-entropy alloys—a review, *Entropy* 20 (11) (2018) 890.
- [54] A. Munitz, M. Kaufman, R. Abbaschian, Liquid phase separation in transition element high entropy alloys, *Intermetallics*. (Barking) 86 (2017) 59–72.
- [55] N. Derimow, R. Abbaschian, Solidification microstructures and calculated mixing enthalpies in CoCrCu containing alloys, *Mater. Today Commun.* 15 (2018) 1–10.
- [56] D. Herlach, R. Cochrane, H. Fecht, A. Greer, Containerless processing in the study of metallic melts and their solidification, *Int. Mater. Rev.* 38 (6) (1993) 273–347.
- [57] A.M. Mullis, O.E. Jegede, T.D. Bigg, R.F. Cochrane, Dynamics of core–shell particle formation in drop-tube processed metastable monotectic alloys, *Acta Mater.* 188 (2020) 591–598.
- [58] W. Nan, W. Bing-Bo, Droplet undercooling during containerless processing in a drop tube, *Chin. Phys. Lett.* 21 (6) (2004) 1120.
- [59] C. Kreischer, T. Volkman, Transformation kinetics of the metastable bcc phase during rapid solidification of undercooled Fe-Co alloy melts, *Materialia* (Oxf) 20 (2021) 101211.
- [60] J. Zhang, Y. Zhang, F. Zhang, D. Cui, Y. Zhao, H. Wu, X. Wang, Q. Zhou, H. Wang, Dendrite growth and grain “coarsening” in an undercooled CoNi equiatomic alloy, *J. Alloys. Compd.* 816 (2020) 152529.
- [61] J. Zhang, X. Li, Y. Zhang, F. Zhang, H. Wu, X.-z. Wang, Q. Zhou, H. Wang, Sluggish dendrite growth in an undercooled high entropy alloy, *Intermetallics*. (Barking) 119 (2020) 106714.
- [62] M. Rahul, G. Phanikumar, Solidification behaviour of undercooled equiatomic FeCuNi alloy, *J. Alloys. Compd.* 815 (2020) 152334.
- [63] W. Wang, Z. Kong, Phase separation and microhardness of rapidly solidified high-entropy CoCrFeNiCu alloys, *J. Alloys. Compd.* 853 (2021) 156451.
- [64] A.F. Andreoli, O. Shuleshova, V.T. Witusiewicz, Y. Wu, Y. Yang, O. Ivashko, A.-C. Dippel, M.v. Zimmermann, K. Nielsch, I. Kaban, In situ study of non-equilibrium solidification of CoCrFeNi high-entropy alloy and CrFeNi and CoCrNi ternary suballoys, *Acta Mater.* 212 (2021) 116880.
- [65] N. Liu, P. Wu, P. Zhou, Z. Peng, X. Wang, Y. Lu, Rapid solidification and liquid-phase separation of undercooled CoCrCuFeNi high-entropy alloys, *Intermetallics*. (Barking) 72 (2016) 44–52.
- [66] T. Guo, J. Li, J. Wang, Y. Wang, H. Kou, S. Niu, Liquid-phase separation in undercooled CoCrCuFeNi high entropy alloy, *Intermetallics*. (Barking) 86 (2017) 110–115.
- [67] K. Lin, C. Wei, Y. He, C. Li, P. Zhang, J. Li, J. Wang, Formation of core–shell structure in immiscible CoCrCuFe_{1.5}Ni_{0.5} high-entropy alloy, *Mater. Lett.* 321 (2022) 132452.
- [68] P. Wu, N. Liu, P. Zhou, Z. Peng, W. Du, X. Wang, Y. Pan, Microstructures and liquid phase separation in multicomponent CoCrCuFeNi high entropy alloys, *Mater. Sci. Technol.* 32 (6) (2016) 576–580.
- [69] C. Cao, D. Herlach, M. Kolbe, G. Görler, B. Wei, Rapid solidification of Cu₈₄Co₁₆ alloy undercooled into the metastable miscibility gap under different conditions, *Scr. Mater.* 48 (1) (2003) 5–9.
- [70] Z. Xia, W. Wang, S. Luo, B. Wei, Liquid phase separation and rapid dendritic growth of highly undercooled ternary Fe_{62.5}Cu_{27.5}Sn₁₀ alloy, *J. Appl. Phys.* 117 (5) (2015).
- [71] A.L. Greer, Confusion by design, *Nature* 366 (6453) (1993) 303–304.
- [72] A. Inoue, Stabilization of metallic supercooled liquid and bulk amorphous alloys, *Acta Mater.* 48 (1) (2000) 279–306.
- [73] A. Takeuchi, A. Inoue, Mixing enthalpy of liquid phase calculated by miedema’s scheme and approximated with sub-regular solution model for assessing forming ability of amorphous and glassy alloys, *Intermetallics*. (Barking) 18 (9) (2010) 1779–1789.
- [74] G. Sheng, C.T. Liu, Phase stability in high entropy alloys: formation of solid-solution phase or amorphous phase, *Prog. Natural Sci.: Mater. Int.* 21 (6) (2011) 433–446.
- [75] H. Lukas, S.G. Fries, B. Sundman, *Computational Thermodynamics: the Calphad method*, Cambridge university press, 2007.
- [76] L.T. Eleno, C.G. Schön, Ternary interaction parameters in calphad solution models, *Brazil. J. Phys.* 44 (2014) 208–214.
- [77] R. Wagner, R. Kampmann, P.W. Voorhees, Homogeneous second-phase precipitation, *Phase Transform. Mater.* (2001) 309–407.
- [78] D.A. Porter, K.E. Easterling, *Phase Transformations in Metals and Alloys* (revised reprint), CRC press, 2009.
- [79] Y. Zhang, Z. Chen, D. Cao, J. Zhang, P. Zhang, Q. Tao, X. Yang, Concurrence of spinodal decomposition and nano-phase precipitation in a multi-component AlCoCrCuFeNi high-entropy alloy, *J. Mater. Res. Technol.* 8 (1) (2019) 726–736.
- [80] K. Binder, P. Fratzl, Spinodal decomposition, *Phase Transf. Mater.* (2001) 409–480.
- [81] J.W. Cahn, Phase separation by spinodal decomposition in isotropic systems, *J. Chem. Phys.* 42 (1) (1965) 93–99.
- [82] D. Stauffer, A. Aharony, *Introduction to Percolation Theory*, CRC press, 2018.
- [83] D. Seol, S. Hu, Y. Li, J. Shen, K. Oh, L. Chen, Computer simulation of spinodal decomposition in constrained films, *Acta Mater.* 51 (17) (2003) 5173–5185.
- [84] H. Nishimori, A. Onuki, Pattern formation in phase-separating alloys with cubic symmetry, *Phys. Rev. B* 42 (1) (1990) 980.
- [85] W. Wang, D. Gong, H. Wang, Y. Ke, L. Qi, S. Li, R. Yang, Y. Hao, Spinodal decomposition coupled with a continuous crystal ordering in a titanium alloy, *Acta Mater.* 233 (2022) 117969.
- [86] A.G. Khachatryan, *Theory of Structural Transformations in Solids*, Courier Corporation, 2013.
- [87] F. Zhu, P. Haasen, R. Wagner, An atom probe study of the decomposition of Fe-Cr-Co permanent magnet alloys, *Acta Metallur.* 34 (3) (1986) 457–463.
- [88] F. Findik, Improvements in spinodal alloys from past to present, *Mater. Des.* 42 (2012) 131–146.
- [89] N.F. Kazakov, *Diffusion Bonding of Materials*, Elsevier, 2013.
- [90] D.E. Laughlin, K. Hono, *Physical Metallurgy*, Newnes, 2014.